Coastal Engineering 213 (2027) 105172

Contents lists available at ScienceDirect

Coastal Engineering

journal homepage: www.elsevier.com/locate/coastaleng

Experimental study on measured erosion resistance of material transitions on dikes due to overflow: hydraulic stability and reinforcement techniques

Ina Schulte [a,*], S. Harish [a], Nils Goseberg [b,c], Holger Schüttrumpf [a]

[a] Institute of Hydraulic Engineering and Water Resources Management, RWTH Aachen University, Mies-van-der-Rohe-Straße 17, Aachen, 52074, Germany
[b] Leichtweiß-Institute for Hydraulic Engineering and Water Resources, Technische Universität Braunschweig, Beethovenstraße 51A, Braunschweig, 38106, Germany
[c] Coastal Research Center, Joint Research Institute of Leibniz University Hannover and Technische Universität Braunschweig, Merkurstraße 11, Hannover, 30419, Germany

ARTICLE INFO

Keywords:
Sea dikes
Transitions
Overflow
Erosion
Damages
Failure mechanisms
Reinforcement techniques

ABSTRACT

Sea dikes exhibit numerous discontinuities due to material and geometric transitions. In the past, these transitions have often led to initiation of damage and even dike failure as they are weak points in the overall dike surface. This experimental study systematically investigates eight different landside slopes, focusing on vertical and horizontal material transitions and their hydraulic stability against overflow. The test variations include different construction methods and building materials, with the ultimate objective of improving transitions from hard to soft materials to reduce erosion. The results show that erosion first initiates at transitions and from there, progressively develops into the slope body, indicating that these areas are erosion-prone. For every model setup tested, changes to construction and other measures, such as the use of erosion control materials and other structural measures, resulted in higher erosion resistance, and the failure criteria were ultimately reached after overflow unit discharges of ~250 l/(s*m) for vegetated dikes with reinforcement measures. Implementing a 3D mesh mat combined with non-woven geotextile proved effective in strengthening transitions and increasing discharge capacity by more than four times for vertical transitions and up to three times for horizontal transitions compared to no improvement measures. The performance of the reinforcement techniques is evaluated, allowing recommendations to be derived for suitable layouts, material combinations, and construction methods to optimize and strengthen future practical designs of transitions on sea dikes.

1. Introduction

Seaward dike slopes are directly exposed to wave impact, wave run-up, and run-down, and their protection systems, such as revetments and other hard armoring measures, are therefore designed for repeated storm-related hydraulic loading in addition to extreme design conditions (EurOtop, 2018; TAW, 2002). Landward sea dike slopes and crests, however, are primarily loaded during rare extreme events, when wave overtopping and steady overflow occur during storm surges, and are thus predominantly designed for ultimate limit state conditions with low exceedance probabilities while being predominantly protected by grass-covered revetments (EAK, 2007; Schüttrumpf and Oumeraci, 2005). Nevertheless, overflow and wave overtopping are among the main causes of dike failure (EurOtop, 2018; van Baars and van Kempen, 2009; van der Vegt et al., 2025), highlighting the need for a detailed investigation of landward processes and associated damage mechanisms.

Many experimental studies focused on the breaching of dikes (Stanczak, 2008; Bernitt and Lynett, 2011; Sanchez-Arcilla, 2006; Zhao, 2016), while others examine surface erosion processes on vegetated dike surfaces during overflow and overtopping (Thornton et al., 2014; Scheres and Schüttrumpf, 2020). However, only limited literature exists on the effect of transition on dikes. Transitions on dikes can trigger erosion initiation and therefore accelerate dike failure (van Bergeijk et al., 2022a). In past storm events, e.g., during the 1962 storm surge (Kolb et al., 1962; Schüttrumpf and Oumeraci, 2002) and Hurricane Katrina 2005 (van Steeg and van Hoven, 2013a), it became clear that transitions are weak points within the dike, thus necessitating systematic analysis of erosion development near transitions, as they may ultimately result in the overall structural failure.

This work defines geometric or material changes on dikes as transitions, and these can be classified into vertical (cross-dike orientation)

* Corresponding author.
E-mail address: schulte@iww.rwth-aachen.de (I. Schulte).

https://doi.org/10.1016/j.coastaleng.2026.105172
Received 29 June 2026; Received in revised form 7 October 2026; Accepted 7 October 2026
Available online 10 October 2026
0378-3839/© 2026 The Authors. Published by Elsevier B.V. This is an open access article under the CC BY license (http://creativecommons.org/licenses/by/4.0/).
Open access funding enabled and organized by Projekt DEAL.

and horizontal (along-dike orientation) irregularities (Schulte et al., 2024; TAW, 1999). Geometric transitions are, e.g., changes in inclination or height differences, while material transitions indicate a change from one cover type to another, such as from grass to paving stones. Previous investigations on transitions on the landward slope of dikes have been based on physical in-situ tests using the overtopping simulator to investigate the influence of transitions on erosion (Steendam et al., 2011). However, many physical overflow and overtopping studies focus on erosion processes on homogeneous material dike surfaces (e.g., van Damme et al., 2016; Scheres and Schüttrumpf, 2020) (see Table A.1), with the geometric transition at the dike toe often representing a primary failure point, while material transitions within the landward slope have received comparatively little attention. The conducted in-situ studies on transitions mostly show erosion processes of operational dike structures; however, only a few studies investigated how transitions can be improved to increase erosion resistance and build more stable transitions (van der Meer et al., 2025). In van der Meer et al. (2025) improvements like concrete tiles, soil stabilization, rounded edges or geogrid were tested to validate possible reinforcement techniques at geometric and material transitions. The results showed that all techniques successfully reinforced the geometric transition from landward slope to berm and the material transition on the landward berm.

1.1. Objective and novelty of study

Many existing studies on dike erosion under overflow or overtopping conditions focus on homogeneous slopes without geometric or material transitions (see Table A.1). Transitions are, therefore, often treated as special cases and have received comparatively little attention.

The aim of this study is to improve the understanding of the overflow-induced erosion at transitions, from erosion initiation to progressive development on landward dike slopes. The specific objectives of this study include: (a) to investigate and understand erosion initiation and progression near transitions caused by overflow, (b) to quantify erosion volumes, erosion rates and hydraulic stability for different vertical and horizontal transition configurations under different structural improvement measures to evaluate the performance of the reinforcement techniques.

A key novelty of this study lies in the systematic physical modelling of landward material transitions under controlled hydraulic loading, which has not been addressed in previous research. Both vertical (three-dimensional) and horizontal (two-dimensional) transition configurations were examined, consistent with existing classifications in literature (Schulte et al., 2024; van Steeg and van Hoven, 2013b). In addition to comparing different protective measures, particular attention was paid to the local embedment and connection details of erosion-control systems at transitions. Such construction details have rarely been considered in experimental studies, and their hydraulic performance under overflow conditions has not yet been systematically tested. The presented results, therefore, provide an initial experimental basis for validating structural improvements and embedment strategies, serving as both an initial step toward practical recommendations and a foundation for future research.

While wave overtopping provides a more realistic representation of natural loading conditions, previous studies have shown that erosion progression is governed primarily by the cumulative hydraulic load associated with the volume of individual overtopping events that exceed the critical erosion threshold, expressed in terms of critical flow velocity in van der Meer et al. (2010a). Similar mean discharges may result from many small or a few large overtopping volumes, whereas large individual volumes are particularly relevant for the initiation and expansion of erosion (van der Meer et al., 2010a; Ebrahimi et al., 2025). However, a controlled overflow approach, as applied in the present study, allows the hydraulic loading to be increased systematically and the resulting erosion response to be investigated, enabling the identification of critical loading conditions. While overflow does not reproduce the unsteady nature of wave overtopping, it provides a suitable method to investigate erosion processes in the vicinity of transitions and to derive practical reinforcement techniques, which is the primary focus of the study. Furthermore, the controlled loading conditions ensure excellent repeatability, allowing future tests to be conducted under identical conditions.

The paper is structured as follows: Initially, a detailed literature review of erosion processes at transitions is presented. Following that, the experimental setup, including the instrumentation, tested flow conditions, and tested landward dike model configurations, is detailed. The results are discussed in detail, based on visual observations and measured erosion depth, volume, and rate for the different setups tested, to highlight the effect of reinforcement techniques. Finally, the discussions on practical applicability and limitations of the study are presented and concluding remarks are drawn.

2. Literature review of erosion processes at transitions due to overflow

When water overflows a dike, it passes through different zones, from the subcritical flow towards the supercritical flow over the crest, and the highly turbulent supercritical flow on the landward dike slope (Fig. 1 a). While in the subcritical zone on the crest, erosion is unlikely; it can be expected at the downstream edge of the crest, where the energy gradient

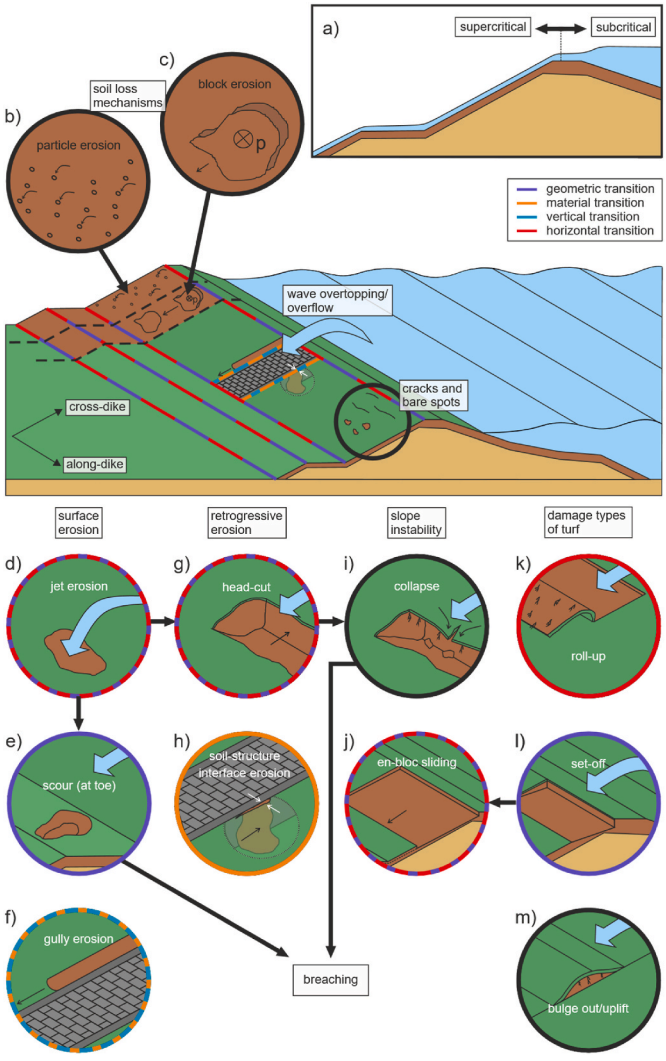


Fig. 1. Schematic sketch of general erosion processes on dikes, with a focus on transitions. The arrows show the potential of a cascading process.

and therefore bottom shear stress are increasing, and negative pressures can occur (Powledge et al., 1989; Nandhini et al., 2026). With acceleration of the flow on the landside slope and an increase in tractive stresses, the erosion potential will rise at the lower dike slope (Pan et al., 2015). Even though the upper landward slope can also be affected by high normal stresses due to flow separation and reattachment of the geometric transition from crest to slope in the case of wave overtopping, depending on the overtopping wave volume and the slope inclination (Ponsioen et al., 2019; van Bergeijk et al., 2022b), the lower landward slope is still estimated to be the most critical location for damage initiation and development (van der Meer et al., 2010b). Therefore, the landward side of the dike will be the focus of the present study.

The external erosion mechanisms described in the following sections are generally based on uniform, homogeneous dike slopes without transitions; however, the same fundamental processes can still govern erosion initiation and progression at transitions within the dike body or at interfaces with structural elements. Transitions may also trigger or accelerate these processes through sudden changes in hydraulic loading, such as increased local flow velocities or turbulence intensities (Hoffmans, 2012). Fig. 1 provides a schematic overview of damage processes on landward dike slopes identified in the literature, categorized into surface erosion (Fig. 1 d–f), retrogressive erosion (Fig. 1 g and h), slope instabilities (Fig. 1 i and j), and turf cover-specific damage (Fig. 1 k–m). Where previous studies identify specific geometric, material, vertical, or horizontal transitions as particularly prone to initiating a process, this is indicated by color coding in the figure. Surface erosion governs initial material loss, while retrogressive erosion and slope instabilities represent subsequent stages affecting structural integrity. Arrows in the figure indicate processes that can initiate others. External surface erosion comprises particle (Fig. 1 b) and block erosion (Fig. 1 c) (Schüttrumpf and Scheres, 2020; Hoffmans et al., 2015).

Once microscopic shear stress or critical flow velocity is exceeded, individual soil particles are gradually loosened and transported, particularly on the middle to lower slope where flow velocities are higher (Fig. 1 b). Block erosion is driven by macroscopic shear forces and affects structurally weaker surface areas, causing discrete soil blocks to detach (Fig. 1 c). Increasing shear stress exposes and removes further weak soil zones in discrete blocks, potentially resulting in large-scale soil loss and dike breaching (Schüttrumpf and Scheres, 2020; Pan et al., 2015). Such structurally weaker zones frequently occur in transition areas due to changes in material properties or geometry. Sudden and non-defined erosion initiation as aggregates is typical for cohesive soils due to interparticle forces, while noncohesive soils erode gradually as individual particles (Utley and Wynn, 2008).

Once erosion initiates on the landside slope, surface discontinuities can alter flow characteristics and trigger cascading erosion. Such discontinuities include bare spots in the grass cover, surface irregularities, and material or geometric transitions (Schüttrumpf and Oumeraci, 2004; Scheres and Schüttrumpf, 2020). Shrinkage and expansion of unsaturated cohesive dike material may cause vertical pull-cracks, which weaken the cover and provide initiation points for further erosion through fissure infiltration (Richwien et al., 2010; Stanczak, 2008; Hoffmans, 2012). Geometric changes, such as small overfalls or changes in inclination, can cause jet erosion (Fig. 1 d) and subsequent scour-hole development at the jet-impact location (Fig. 1 e) (Verheij et al., 2012; Ponsioen et al., 2019; van Bergeijk et al. 2022a, 2022b). Although cohesive slopes are generally more erosion resistant than granular materials (Hoffmans, 2012), scour initiation at the dike toe can still lead to lateral and upstream propagation and slope undercutting (Powledge et al., 1989). The dike toe is considered one of the most critical locations for the initiation of scours in previous dike overtopping experiments (van der Meer et al., 2010b; Steendam et al., 2011). While jet erosion is mostly locally concentrated and scour is areal, gully erosion is a linear surface-erosion process that develops downstream (Fig. 1 f). A concentration of flow along a structure (e.g., staircase, ramp) can initiate gully erosion (van der Meer et al., 2010b; Kolb et al., 1962).

Retrogressive erosion describes erosion processes propagating upstream, often counter to the main flow direction (van der Meer et al., 2012). Head-cut erosion is a typical form of retrogressive erosion on landward dike slopes (Fig. 1 g), where a local scour forms a steep erosion face that progressively migrates upslope through undermining and collapse, potentially leading to breaching (Pinettes et al., 2025; van der Meer et al., 2012; Depreiter et al., 2025). Soil-structure interface erosion (joint erosion) can similarly develop retrogressively (Fig. 1 h). At transitions between rigid structures and the adjacent earthwork, preferential seepage and flow concentration increase hydraulic gradients and shear stresses, promoting particle detachment, internal material transport, and cavity formation (MMB, 2013; DWA-M 507-1, 2011; Xie et al., 2018; Chen et al., 2022). Hydraulic conductivity at such soil–structure interfaces can be up to 2.78 times higher than in intact soil, indicating preferential flow paths (Zhang et al., 2025).

A grass layer provides an initial protection against erosion and stabilizes the underlying cohesive soil (Hoffmans, 2012; Sprangers, 1999; Igwe et al., 2017). Nevertheless, scour and head-cut erosion can still occur, alongside turf-specific mechanisms such as roll-up, bulging, and set-off occur (Le et al., 2017; Steendam et al., 2012; Kolb et al., 1962; Hewlett et al., 1987). Exposed turf edges can be lifted and torn by drag forces, causing roll-up (Fig. 1 k) (Le et al., 2017), while seepage beneath the grass cover can cause uplift or bulging (Fig. 1 m) (Hewlett et al., 1987). Turf set-off can result from cracking or degradation beneath the crest, causing saturated soil to subside and the turf to detach as a block (Fig. 1 l) (Kolb et al., 1962; Oumeraci et al., 2001). Local uprooting may occur at weak or uneven grass cover, although the root network can remain intact (van der Meer et al., 2012). Turf-related damage mechanisms may both initiate erosion locally and accelerate the transition from surface erosion to slope instability. At transitions, degradation may accelerate due to flow concentration and reduced root continuity.

Slope instability represents a subsequent stage of the erosion–failure cascade, often triggered by preceding surface or retrogressive erosion. Material removal, toe undercutting, or increased pore water pressures can reduce slope stability. Collapse involves sudden failure of undermined soil masses (Fig. 1 i), e.g., at scour holes or head-cuts (Le et al., 2017). En-bloc sliding describes the movement of coherent soil or turf blocks along a slip surface (Fig. 1 j) and can lead to rapid partial or complete breach (Schüttrumpf and Oumeraci, 2004; Kolb et al., 1962). After turf set-off is initiated on the landward dike slope, it can be followed by en-bloc sliding due to the prolonged infiltration of overtopping water, which reduces the stabilizing effect of the grass. Slip erosion (not pictured in Fig. 1) is associated with steep slopes (steeper than 1:2) (van der Meer et al., 2010b) or with material changes in a distinct slip plane within the dike structure (Olschewski et al., 2015). At transitions, these slope instability mechanisms may develop faster due to stiffness contrasts, geometric irregularities, reduced continuity of soil and root structures and concentrated flow paths.

While those processes described above are all erosion and deterioration mechanisms that govern damage initiation and progression, their interaction may ultimately result in breach formation as the final failure state. As most mechanisms have been studied for homogeneous dike slopes, erosion at geometric and material transitions requires further consideration. This study therefore focuses on erosion and damage initiation at the dike surface near transition areas.

3. Material and Methods

3.1. Experimental facility and model configurations

The overflow tests were conducted in the 2 m wide dike model located in the laboratory of the Institute of Hydraulic Engineering and Water Resources Management, RWTH Aachen University, Germany. Before the water reaches the actual test flume, it is calmed in a large inlet basin to ensure that the incoming water experiences only minor fluctuations. As soon as the water level in the inlet basin reaches the height

of the model dike crest, overflow of the dike occurs.

The model represents an unscaled section of a classic sea dike with a landward embankment of 1:3 slope inclination (EAK, 2007; TAW, 1999; CIRIA, 2013). The landward slope and the crest are represented in the model, while the seaward slope is not modelled. Since the flow processes on the surface of the dike are particularly relevant for the tests, and flow processes inside the dike are not to be considered, the dike is separated from the inlet basin by a sealed wall so that seepage through the dike does not occur. The dike core was made out of washery refuse, which forms the base for the 0.5 m thick cohesive covering layer of the dike. The total height of the dike is 2 m. The crest width of the model dike is 2.1 m, and the slope has a total length of 5.4 m. The dike covering material used for the laboratory dike construction is a clayey silt, chosen based on local availability. Nevertheless, it still shows conditionally suitable properties like the clay traditionally used in northern Germany for dike construction (Achmus et al., 2019; EAK, 2007) and is classified as clay with little erosion resistance according to the Dutch standards (TAW, 1996). A comparison of characteristic values of the material composition specified by the German guideline EAK (2007), values from previous studies and from the clay used in this study can be found in Table A.2. Fig. 2 presents the three soil samples of the dike construction material that were tested using sedimentation and sieving in accordance with the German norm DIN 18123-7 (DIN 18123-7, 2011) (probe 2 and 3) and laser diffraction (probe 1).

In total, eight transition configurations (V1-V8) were tested during the investigations (see Fig. 3). The transition configurations are categorized according to the approach of Schulte et al. (2024) where the orientation of the transition in the cross-dike x (vertical) and along-dike z (horizontal) direction is decisive. In these experiments, one reference setup (V1), four setups with vertical transition (V2-V5), and three setups with horizontal transition (V6-V8) were investigated.

The material was laid in layers 10–20 cm thick and compacted. Compaction was carried out parallel to the slope gradient using a vibrating plate in each case, which was passed over the entire surface 3-4 times. In areas close to the transition/dike installations, the clay was also manually compacted with a hand-operated tamper until no further visual compression was observed. The installation in the model differs from reality in that no large machines can be used. In large dike construction projects, the clay is pressed down with bulldozers and sheep's foot rollers in layers 30–50 cm thick, applying as much surface pressure as possible (EAK, 2007). For each new dike construction (except V2 and V3), the top 30 cm of the clay cover was removed and rebuilt from there, which was the deepest cut after erosion from the previous tests. For the V2-V3 tests, only the eroded areas were repaired locally and not rebuilt and compacted over a large area; further details can be found in Chapters 4.1.1 and 4.2.1 The clay was prepared accordingly and reused before each new construction.

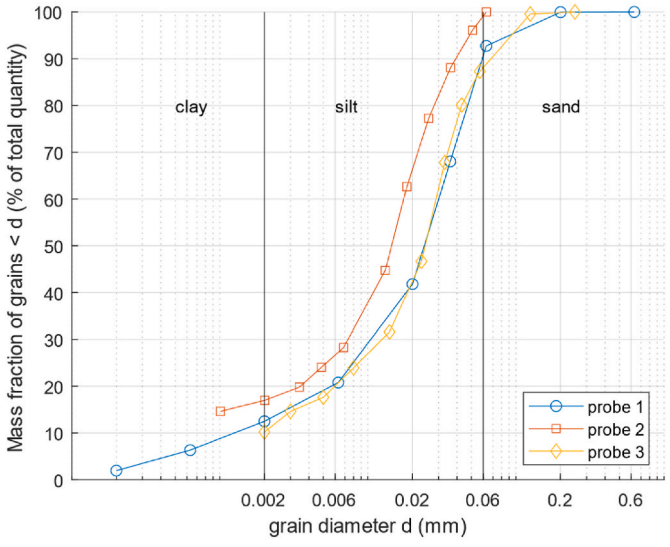


Fig. 2. Gradation curves of the clayey silt used as dike covering material in the model tests.

During dike construction, quality controls were carried out to verify the degree of compaction. The core cylinder method, as specified in DIN 18125-2 (DIN 18125-2, 2020), was employed for this purpose. For cohesive cover soils, the minimum value of the Proctor density ρ_{Pr} for the degree of compaction should be $D_{Pr}\geq 95\%$ (EAK, 2007) or $D_{Pr}\geq 97\%$ (DIN 19712, 2013). The Proctor density for the covering material was $\rho_{Pr} = 1.753\ g/cm^3$. Overall, an average density of $D_{Pr} = 102.4\%$ was achieved during model setup. This value is a mean from spot checks taken in different layer depths and during every reconstruction of a new setup, not including any repaired areas.

The classic grass cover of green sea dikes was neglected in most investigations aimed at understanding the initiation of damage at transitions, so the conservative assumption of an unvegetated dike was considered sufficient. However, in V5, rolled turf was added to understand the additional effect of the vegetated top layer on the erosion resistance compared to the simplified clay surfaces. In the past, numerous studies have also been conducted on vegetated revetments (see Table A.1), allowing for direct comparison with a classic green sea dike.

The various structures were planned as a sequence of different systematic installation steps leading up to a realistic construction of a more erosion-resistant and stable dike, including the implementation of different measures that help to prevent erosion at transitions from hard to soft covers. Looking at the plan views of the slope surfaces for the different tests V1-V8 in Fig. 3, the following considerations for the systematic test setup should be highlighted:

a) V1 represents the reference case of a dike that does not exhibit any material transitions from hard to soft. Only the model walls are present here, which can also be regarded as a transition (e.g., a building in the dike).
b) In V2, paved edge areas with a width of 0.5 m were added, to create a vertical transition. The paved areas (stone dimensions 20 × 10 × 8 cm) were laid on an approx. 2 cm thick gravel bed (grain size 2-8 mm) so that they were level with the adjacent bare soil. For sections V2 through V5 (vertical transitions), in addition to the flat paved area on the slope, the paving stones were extended 0.5 m beyond the dike slope toe into the area of the horizontal berm.
c) V3 is a replication of V2 with the addition of curb stones (stone dimensions 100 × 30 × 8 cm) to enclose the paved areas along the slope.
d) In V4, the middle part of the clay is reinforced by a biodegradable 3D mesh mat and mechanically consolidated non-woven fabric (400 g/m^2) in the transition area, which is intended to improve the transition from hard to soft. Looking from the toe of the dike upwards, two different installation methods for the mesh and the fabric were implemented. On the left side, the fabric was embedded along the curb stones for 17 cm in the vertical direction and extended for another 12 cm on the horizontal plane. The fabric was laid 5 cm below the dike surface along the whole cross-dike line. On top of the fabric, the mesh was installed flush with the edges of the curb stone and fastened at intervals of 50 cm along the cross-section of the dike with ground nails (U-clamps of 23 cm length). On the right side, the mesh was coated with the fabric and also firmly and wrinkle-free embedded for 17 cm along the curb stone (see section view A-A in Fig. 3). While the left-hand method promises easier installation and less loosening of the soil structure, the mesh is only held in place by the U-clamps, and there is no direct connection to the adjacent hard curb stone. The right-hand method embeds the mesh directly, preventing undermining at the edges and destabilization. To also prevent the formation of a drainage channel along the deep curb stones

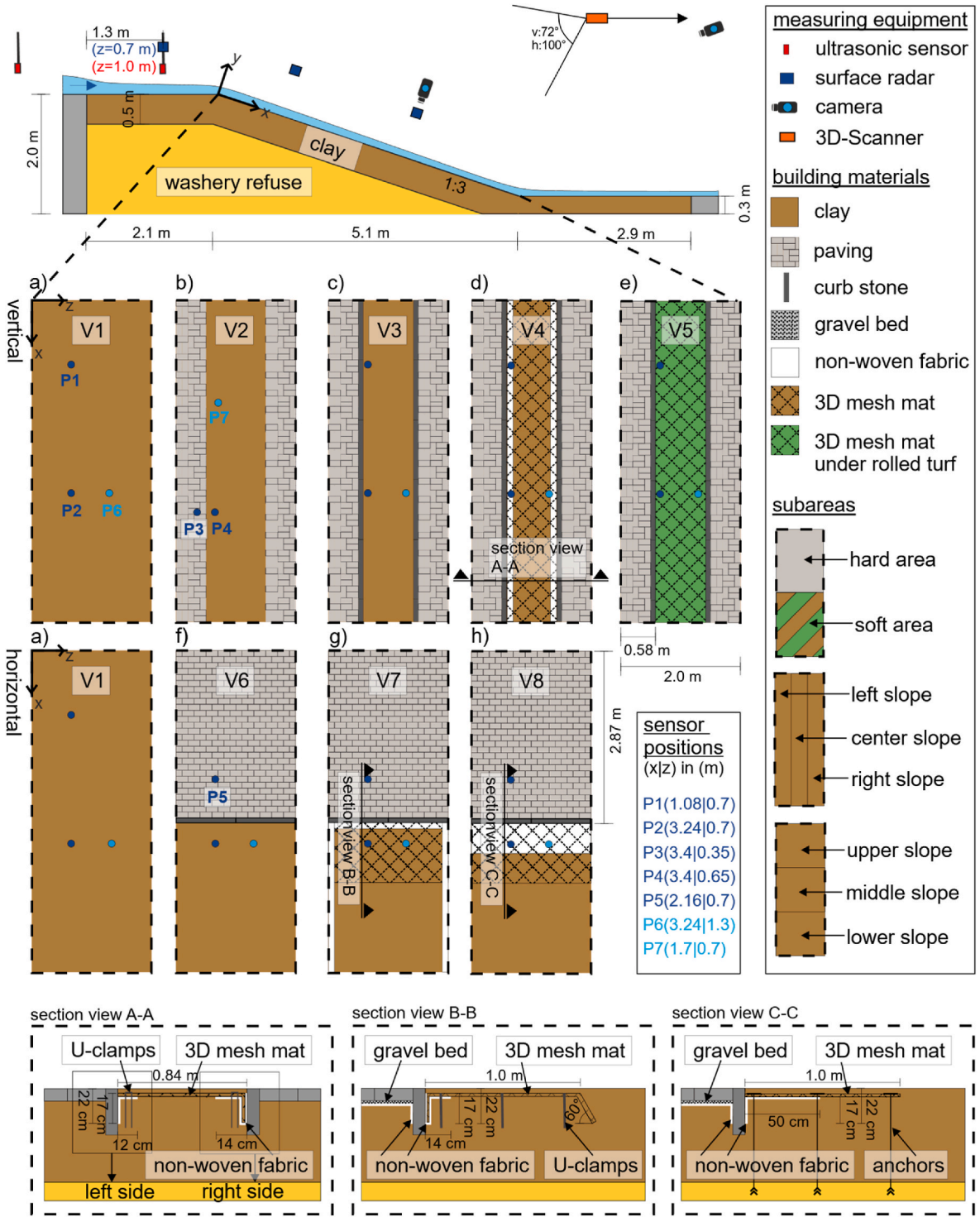


Fig. 3. Test setup with measuring positions and the model configurations V1-V8.

due to the open structure of the mesh, it is essential to use geotextile fabric as a covering with this method, as careful filling and compaction of the 3D structure in the edge area is not practicable. Root penetration of thin, open-pored non-woven fabrics is also possible, so that the continuity of the turf is not impaired but rather reinforced by the additional installation of erosion control products. In the V4 setup, the bedding with gravel under the paving was omitted, and the concrete blocks were laid directly in the clay.

e) In test setup V5, the structure of V4 was reproduced, with the addition of rolled natural turf on the 3D mesh mat. The dimensions of the turf rolls were 173 × 58 cm, allowing them to be laid with an offset and only cut to size lengthwise. The turf was allowed to grow for more than 7 weeks, developing roots that penetrated the ground and surrounded the 3D mesh mat. Based on the root development phases reported for grasses by Robin et al. (2021), which include rapid root elongation within the first 10 days and intensive lateral root formation between 10 and 25 days after initiation, a seven-week establishment period can be considered sufficient. The growth of the rolled turf in the laboratory was supported by regular watering and LED lighting, following the approach of Mozer et al. (2024). The

grass was mowed every 2 weeks to a length of 8 cm, which was also the final height for the experiments (Fig. 4). Additionally, a toe protection on the berm against sliding of the paving was installed in the form of two wooden plates (50 × 25 cm) for V5, which were rammed into the soil immediately behind the end of the paved area (see Fig. 12 b and c).

f) V6 states the first test with a horizontal transition (Fig. 3). The crest and upper slope area were paved up to $x = 2.87$ m to create a horizontal transition from hard to soft in the direction of flow. The paved area was bordered by two deep curb stones over the whole dike width. The concrete paving blocks were laid directly in the clay. The transition to the clay covering layer was made level in every horizontal transition test configuration.

g) For the setup V7, the layered structure of the paving stones consisted of a non-woven fabric (200 g/m^2) and an approx. 2 cm thick gravel layer on which the paving stones were laid (see section view B-B in Fig. 3). The clay was also reinforced with a biodegradable 3D mesh mat for a length of 1 m. The mesh was secured over the entire surface at intervals of approx. 50 cm using 23 cm long U-clamps. Building on the improved effectiveness of the installation method on the right-hand side of test V4-V5, the mesh was again covered with a non-woven fabric and integrated along the deep curb stone. At the lower edge of the mesh mat, it was embedded into the soil by a 60° inclined embedding trench over a depth of 17 cm (see Fig. 5 a and section view in Fig. 3). In addition to horizontal integration, non-woven fabric was integrated transversely along the model walls to a depth of 22 cm below the dike surface, laid on the dike surface with a 12 cm overlap, and secured with U-clamps to strengthen the model walls.

h) In V8, the layered structure under the paving stones was kept as in V7. For V8, another material as well as installation technique for the erosion control product of the clay was chosen. A synthetic polypropylene 3D mesh with geogrid mat was used as a reinforcement downstream of the transition. It was placed 5 cm beneath the upper edge of the final dike over a length of 1 m, similar to V7, and anchored with an associated system of five anchors, in accordance with the recommendation of one anchor/m^2, ensuring that all four corners were fastened as well. After tensioning, the anchors were embedded in the ground to an average depth of 35 cm. In addition to the anchors, U-clamps were used at the edges of the mat, as the 3D mesh mat was not embedded in the ground via binding trenches. Underneath the 3D mesh mat, a non-woven fabric was embedded along the curb stones for 17 cm and then applied over 50 cm as a direct base for the 3D mesh mat, ensuring it was flat and wrinkle-free (see Fig. 5 b and section view in Fig. 3).

3.2. Instrumentation and test program

The hydraulic load on the dike is measured using two ultrasonic water depth measuring probes (microsonic, series mic+340/IU/TC in the inflow and pico+35/I on the dike crest), three flow velocity measuring surface radars (Kisters, series HyQuant L + V), and two cameras (GoPro, series HERO8 Black). Additionally, the erosion processes on the dike surface are recorded using a 3D-scanner (Faro, series FocusM70), which is particularly relevant to the results discussed in this study.

While the ultrasonic probes measured with a frequency of 10 Hz during the experiment duration to capture water depths and discharges on the dike, the surface radars were only able to measure at 1 Hz. Originally, surface radars were not used for turbulent and high-velocity discharges, so the results are to be seen as a trial and proof of the measuring technique. The cameras were used to capture the flow of the whole dike slope as well as a detailed excerpt normal to the slope from above the flow. The cameras were able to record 100 fps with a linear lens and a resolution of 1 080 × 1920 px. For the 3D-Scanner, the surface erosion was captured from at least 2 positions after every test. The scan resolution was 5 689 × 4 096 Pt for a horizontal opening angle of 130°-230° and a vertical opening angle of −62°-10°. For the analysis of erosion volumes, only the slope was considered and not the crest and horizontal berm at the toe. The scanning grid was evaluated with a resolution of 5 mm.

The test program is based on the investigations by Scheres and Schüttrumpf (2020). To determine the initiation of damage, the progression of damage, and the resulting critical loads, the test program has been adapted so that the load is increased gradually, in the same way for every model configuration tested. The individual load levels were interrupted at intervals of 10-15 min to scan the dike with the 3D-Scanner and utilize this data in further analysis to determine erosion depth and volume curves, as well as erosion rates (see Section 3.3). Before scanning, water had to drain or seep into the ground for smaller erosion holes, and in cases of scour at the toe of the dike, a pump was used to remove the water to reduce inaccuracies in LiDAR scanning. As soon as a critical degree of erosion was observed, characterized by critical erosion depths (here, approximately 30 cm) or the failure of the hard revetment, up to and including the risk of complete top layer removal, the test series was terminated. The failure criterion of 30 cm was selected based on three considerations: (1) laboratory model constraints, as the lower slope area is located only 30 cm above the flume bottom; (2) the erosion depth had to remain below 50 cm to ensure that the dike core remained unaffected; and (3) the embedment depth of the curb stone. The time measurement started when the water front was observed at the ultrasonic sensor on the crest, which means that, depending on the discharge, it took some time until a quasi-steady state was reached. After the water



Fig. 4. Growth phase of grass for V5: a) installation setup with LED-lamps and irrigation system with damp bottom area, b) final grass length before testing, c) section of grass development on the middle slope.

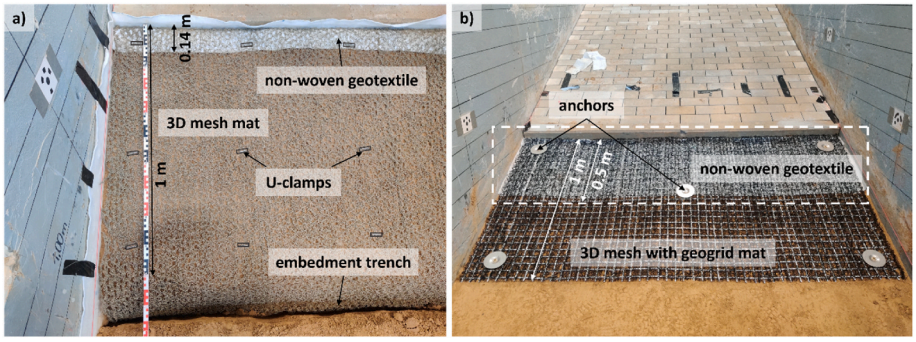


Fig. 5. Different construction and integration methods of 3D mesh mat before 5 cm clay layer was added on top: a) setup in V7 with coating of the 3D mesh mat with the non-woven geotextile at the curb stone and embedment trench (U-clamp positions are highlighted with grey boxes), b) setup in V8 with integration of a non-woven geotextile for half the length of the 3D mesh with geogrid mat and the fastening with anchors.

discharge was turned off again, a trailing wave was observed, prolonging the duration of water overflow. Overall, the discharge q_w (l/(s*m)) was determined based on water level measurements in the inflow area of the flume behind the vertical wall separating the dike section model from the inflow using the Poleni weir overfall equation (1):

$$q_w = \frac{2}{3} \cdot \mu \cdot \sqrt{2 \cdot g} \cdot h_{ü}^{\frac{3}{2}} \tag{1}$$

with μ assumed as 0.5 (Zanke, 2013; Krebs, 2023) and $h_{ü}$ being the overflow height. Table 1 lists the test program carried out. The check marks indicate that the full set of tests per load level was carried out, while the experimental number S indicates the final test per specific setup V before the dike failure criteria were met.

In Fig. 6, the specific steady discharge per experimental run was plotted over time, showing, especially for smaller discharges, some differences in the load levels. However, comparing the measured surface velocities on the dike crest shows that they match very well across the different setups (see Figs. 20 and 24). To better compare the different test scenarios, the load is analyzed over the cumulated water volume V_{cum} overflowing the dike.

3.3. Data analysis

The terrestrial 3D laser scans were first post-processed using FARO® SCENE software to obtain a single registered point cloud of the inner dike slope for each experimental state S and test setup V within a common coordinate system. Subsequently, the original high-resolution point clouds were interpolated onto a uniform 5 mm × 5 mm x-z raster for computational efficiency. As each experimental state represents a scan acquired after a partial loading, the erosion development was evaluated incrementally with respect to constant discharge conditions or, equivalently, the cumulative overflow water volume.

The cumulative erosion volume V_e was determined from the summed soil volume loss between consecutive experimental states by integrating the erosion depth over the raster cells, i.e., erosion depth multiplied by the raster cell area (25 mm^2). Since the erosion of the soft dike-covering material was of primary interest, the calculation of V_e focused on the erodible surface areas (soft area), excluding paved areas. The excluded paved areas comprised the lateral edges in the vertical transition setups ($z < 0.5$-0.58 m and $z > 1.42$-1.5 m) and the upper half of the slope ($x < 2.87$ m) in the horizontal transition setups (Fig. 3). Depending on the setup, that means for the vertical transitions: for V2, after deducting 1 m for the width of the paving stones, 1 m of clay soil remains; and for V3-V5, after deducting a further 16 cm for the width of the curb stones, 84 cm in the middle of the dike remains covered with clay. Additionally, the total slope area, including paved areas, was considered to assess overall erosion development at the end, although the experiments primarily focused on the erodible area.

The maximum erosion depth $d_{e,max}$ was evaluated over the total slope surface, including paved areas, as well as only the soft area and corresponds to the maximum local erosion depth reached for each experimental number S. The mean erosion depth $d_{e,mean}$ was calculated as the mean surface displacement in y-direction (see Fig. 3) along cross sections in x-direction for vertical transitions and along cross sections in z-direction for horizontal transitions.

The erosion rate was evaluated according to $E_i = \frac{\Delta V_i / A}{\Delta t_i}$ with unit of cm^3/(s*m^2), where ΔV_i denotes the erosion volume per test, A the erodible soft-surface area, and Δt_i the corresponding test duration. The erosion rates were analyzed both for individual experimental numbers and across the different hydraulic loading levels represented by the mean discharges.

The time series of surface velocity data recorded by the surface radar were each averaged to a single value per load step v_{mean}. The measurements were done on the crest and at two positions along the slope. For

Table 1
Test program for overtopping flow tests indicating the final experimental number S and duration of testing for each test.

Mean discharge q_w (l/(s*m)) – load level	5	10	22	34	44	68	96	136	170	195	250
Experimental number S	*S1-S4*	*S5-S8*	*S9-S12*	*S13-S16*	*S17-S20*	*S21-S23*	*S24-S26*	*S27-S29*	*S30-S32*	*S33-S35*	*S36-S38*
Test duration t (min)	45	45	45	45	45	30	30	30	30	30	30
Test duration t per experiment S (min)	*S1-S3*: 10 *S4*: 15	*S5-S7*: 10 *S8*: 15	*S9-S11*: 10 *S12*: 15	*S13-S15*: 10 *S16*: 15	*S17-S19*: 10 *S20*: 15	*S21-S23*: 10	*S24-S26*: 10	*S27-S29*: 10	*S30-S32*: 10	*S33-S35*: 10	*S36-S38*: 10
V1	***S3***										
V2	✔	✔	***S9***								
V3	✔	✔	***S9***								
V4	✔	✔	✔	✔	✔	✔	***S26***				
V5	✔	✔	✔	✔	✔	✔	✔	✔	✔	✔	***S36***
V6	✔	***S6***									
V7	✔	✔	***S9***								
V8	✔	✔	✔	***S13***							

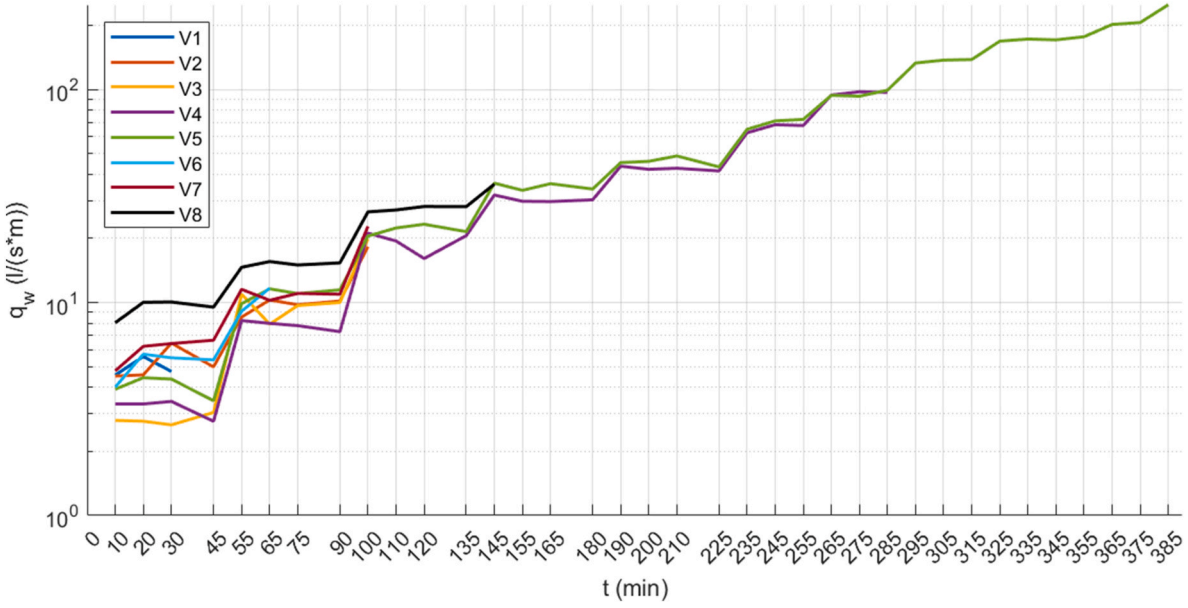


Fig. 6. Steady discharge over time for different experiment configurations, not considering the interruptions to the tests with inflowing and outflowing waves.

experiment V2, the distance from the crest was the same for both sensors, but the position in the along-dike direction differed in that one sensor measured the surface velocity above the pavement, and one sensor measured the velocity above the middle clay area (see Fig. 3). For the remaining experiments with vertical transition, the measuring positions were located at 1/5 and 3/5 of the total slope length.

4. Results

4.1. Observation of erosion processes

4.1.1. Vertical transitions

For all experimental setups, progressing erosion was observed, especially in transition areas. Due to the sequence of construction setups for a more erosion-resistant dike, the results confirmed the expected increase in testing duration with each setup, while the dike became more stable overall. In Fig. 7, an overview of photographs taken before and after testing, along with a color plot of the erosion depths on the dike slopes after the final test status for each vertical setup, is presented. The experimental number *S*0 indicates the pre-scan of every model configuration before any water overflows, which is compared with the erosion after the testing time and the final experimental number.

a) V1: reference test

For reference test V1, the dike was overflown for a total of 30 min before the failure criterion was met (Fig. 7 b). Erosion initiated, particularly in the area of shrinkage cracks that had already formed, primarily in the along-dike direction, before the start of the experiment. Shrinkage cracks are a common physical process that occurs in clay slopes (Stanczak, 2008; Richwien et al., 2010). It was also evident that erosion had increased in the area of the model walls, showing high turbulence and aerated flow (Fig. 8 a). With the erosion starting at the cracks and walls, it progressively developed in layers, coinciding with the sequence of compaction during construction, and hollowing to a depth of 30 cm was observed in the area of the lower right slope on the model wall (Fig. 8 b). In the first test setup, the right side of the model was disrupted by cable ducts, but these were relocated to the subsoil of the dike during further experiments.

b) V2: with paving

Dike setup V2 ultimately failed due to the failure of the paved area near the wall and at the geometric transition from the crest to the upper slope (Fig. 7 e). Erosion began along the paving stones, likely due to the construction process. After repairing V1, the excavation for the paving stones left small gaps between the stones and the adjacent clay, providing preferential erosion paths (Fig. 9). Additional erosion developed at shrinkage cracks, and local erosion pits developed. Undermining on the left-hand side paved area started after 20 min at a discharge of about 5 l/(s*m) (see Fig. 9 a), but settlement remained limited until about 75 min. During the final three partial loads, rapid erosion of the gravel bedding and clay material also developed on the right-hand side, leading to test termination after 100 min at a discharge of approximately 22 l/(s*m). The experiments show that the paving reinforced the wall-adjacent edge areas compared to V1 and delayed wall-induced erosion. However, the paving introduced a new vertical material transition, shifting erosion towards the interface between the stones and the clay. Furthermore, the stone edges altered the flow paths, concentrating the flow within paving joints and adjacent clay areas. The resulting local collapse of paved sections promoted undermining and concentrated flow, which further accelerated erosion (Fig. 9 c).

c) V3: with paving and curb stones

In test V3, 30 cm deep curb stones were installed along the paving to constrain paving movement and undermining. Compared to V2, the revetment experienced overall less settlement, particularly on the upper slope, likely due to clamping between the flume walls and the curb stones as well as the improved interlocking of the paving stones. Nevertheless, the revetment was still significantly undermined and destabilized. Erosion at the crest and along the curb stones was more severe than in V2. An initial erosion rate of at least ~28 $cm^3/(s*m^2)$ was observed within the first seconds of testing at a discharge of about 5 l/(s*m). Locally repaired areas of the dike were eroded directly, since the material integrity and compaction could not be fully restored. The material was eroded into small chunks (block erosion), which were detached from the overall structure (Fig. 10 a and b). The excavated and recompacted trenches required for curb stone installation during

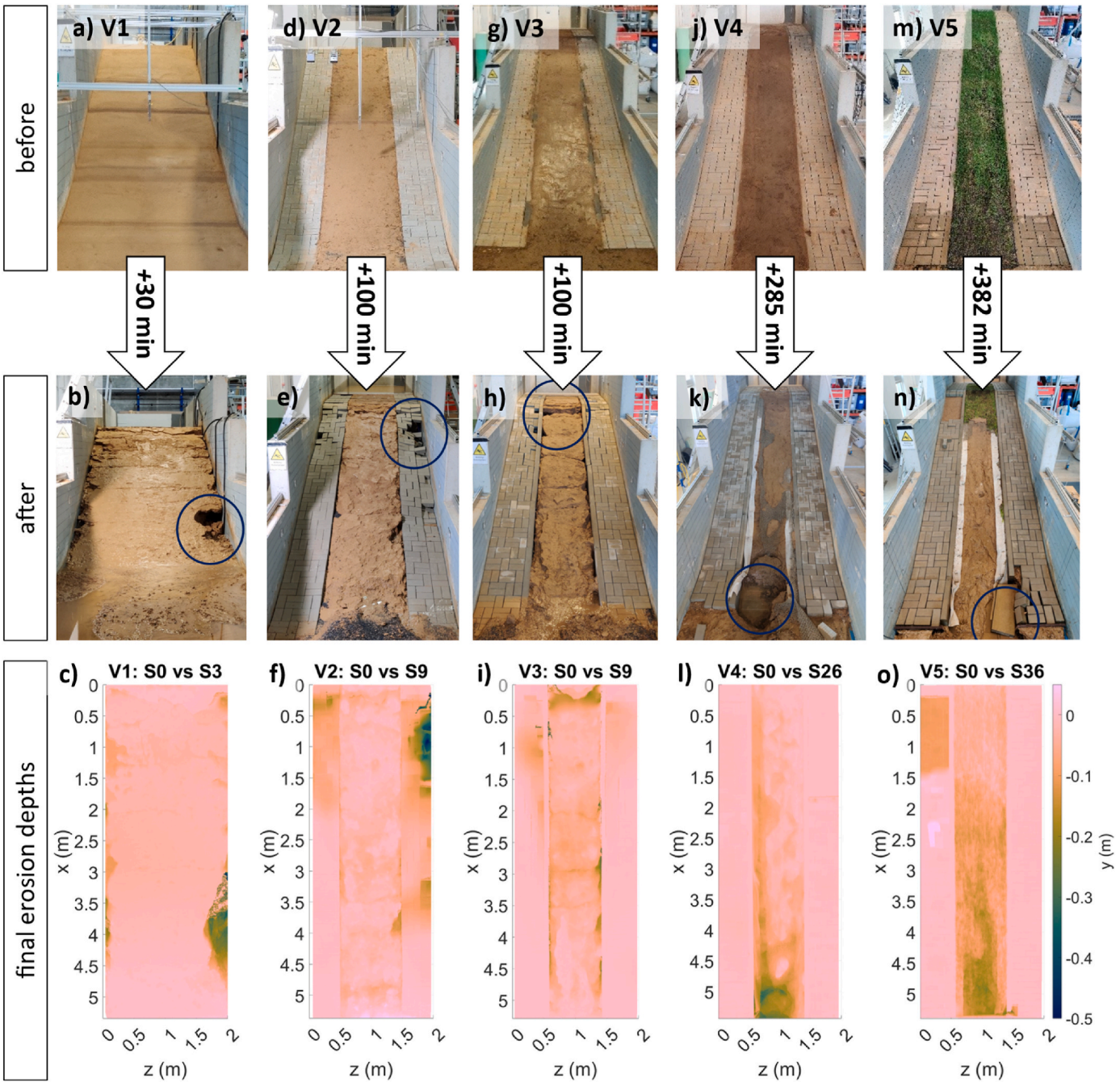


Fig. 7. Initial and final state before and after testing and difference plots of landward dike slope after final testing vertical transition setups a)-c) V1, d)-f) V2, g)-i) V3, j)-l) V4, m)-o) V5 with the testing time for each configuration and the final experimental number S; the circular markings indicate the location where the critical erosion depth as termination criterion was reached.

construction also created preferential erosion zones in the crest and upper slope area, which became evident after removal of the paving (Fig. 10 e). Water infiltrated through the paving joints on the crest, eroding the gravel bedding underneath the stones and promoting interflow beneath the revetment. Without an effective filter layer, this caused progressive undermining. The final failure was characterized by deep erosion of the upper slope, which was no longer concentrated only at the transitions. The observed damage processes resembled head-cut erosion, with initiation at a crack and soil–structure interfaces followed by progressive loss of support beneath the downstream crest and eventual collapse.

d) V4: with paving, curb stones and 3D mesh mat

After locally repairing and extending the experimental setups for V2-V3, the dike surface was renewed completely for the model configuration V4. With the implementation of the 3D mesh mat and non-woven textile at the curb-stone, a clear increase in loading duration up to 285 min with a final load level of approximately 96 l/(s*m) was reached. The erosion developed more uniformly than in the previous experiments, but still, roughening of the soft surface and erosion pit development were observed (Fig. 11 a). Erosion in the transition areas was limited to the level of the non-woven textile, which was only undermined at the bottom left side of



Fig. 8. Photographs during the experiments V1 looking from upstream down the slope: a) during overflow with cable ducts on flume walls and high turbulence at the walls, b) erosion in layers and hollows of up to 30 cm in shrinkage crack areas.

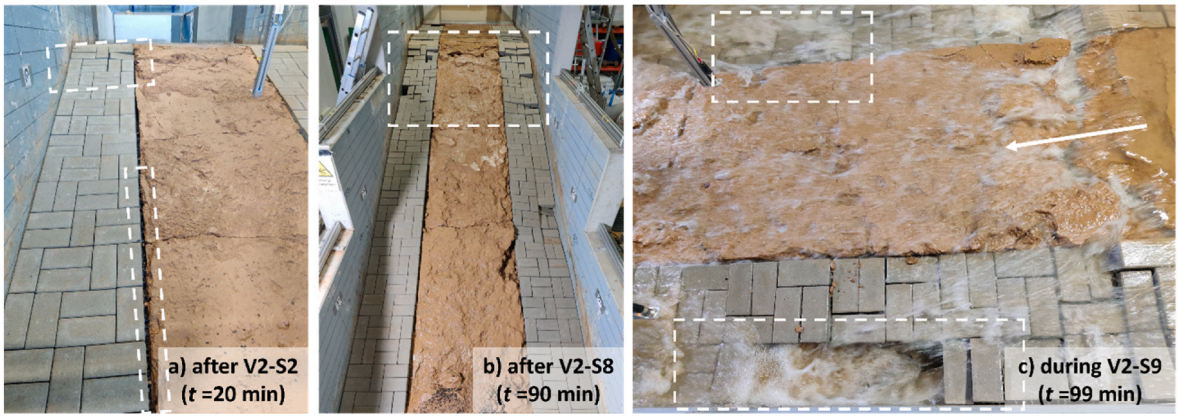


Fig. 9. Photographs during the experiments V2: a) gap between paving and clay and start of undermining of paving stones looking from downstream up the slope, b) collapse of paving stones at inner crest line looking from downstream up the slope, c) undermining of paved areas and redirection and diversion of flow due to stones during overflow in upper slope area (flow direction from right to left).

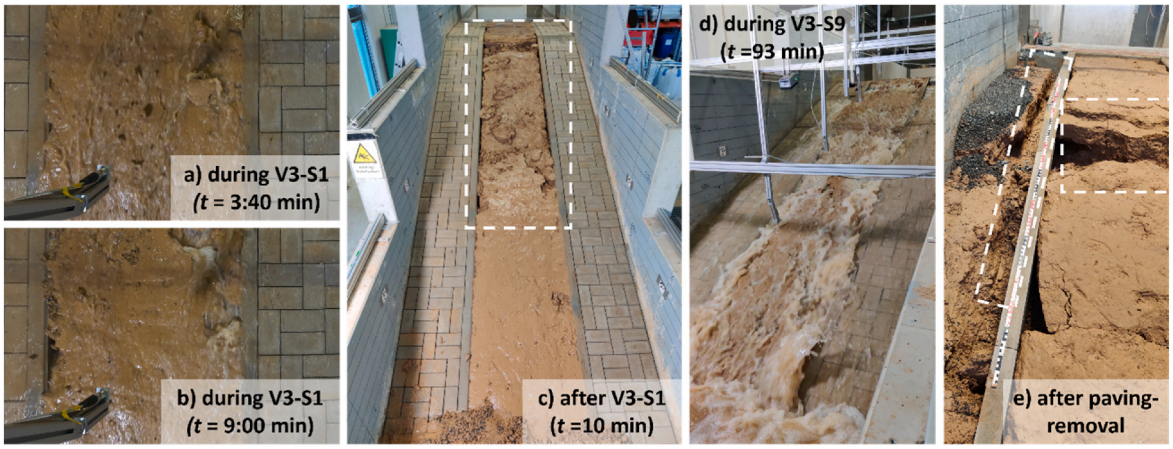


Fig. 10. Photographs during the experiments V3: a), b) development of flow and erosion in small clay chunks at middle slope from above the surface (flow direction from top to bottom), c) heavy erosion after first partial load in upper slope area looking from downstream up the slope, d) high turbulence of flow in material transitions, e) erosion of embedment trenches of deep curb stones after removal of paving stones in upper slope and crest area as well as head-cut erosion at the inner crest line.

the dike. The altered erosion pattern demonstrates the impact of the erosion protection measure. Due to different installation methods of the 3D mesh on the left and right sides between the curb stones, the right-side method showed higher erosion resistance than the left-side method. After 210 min and a loading of approximately 44 l/(s*m), the 3D mesh was first torn off in the lower left side slope right at a rigid U-clamp (Fig. 11 b). With higher loading, the erosion at the left side curb stone moved upward, similar to the demolition of the 3D mesh mat. Shortly before the tests were terminated (after 275 min), sliding of the paving stones on the left side slope was observed (Fig. 11 d). The experiment was finally terminated

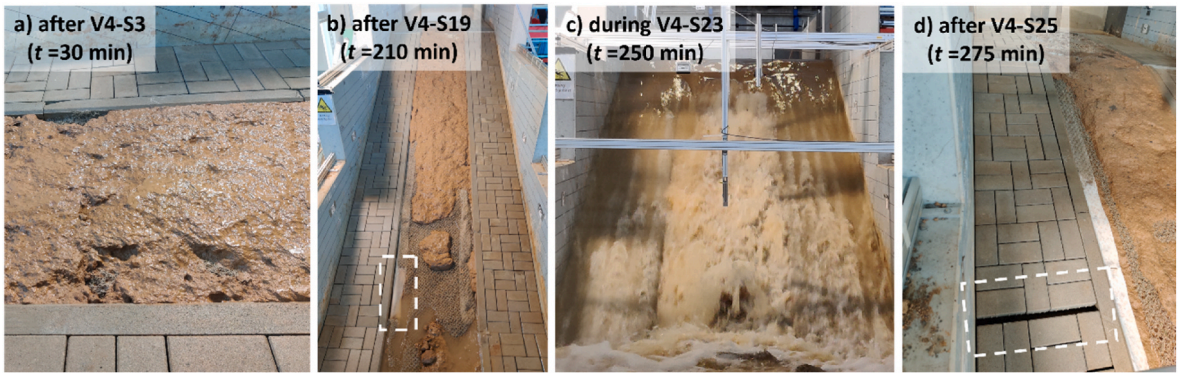


Fig. 11. Photographs during the experiments V4: a) first erosion spots of soil above 3D mesh, b) first demolishment of 3D mesh, c) air-entrainment due to concrete stone joints and irregularities in clay area, d) sliding of the pavement on the slope.

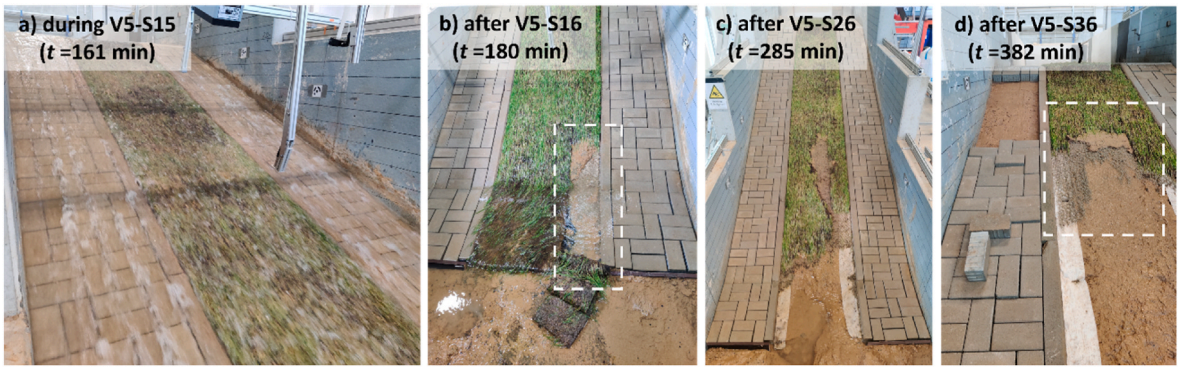


Fig. 12. Photographs during the experiments V5 looking from downstream up the slope: a) flow developed over whole flume width and grass is completely deflected and submerged, b) first erosion of turf at lower slope and toe protection of paved area, c) erosion of turf moving upstream along cut edges of the turf, d) erosion of layers with top to bottom turf, clay, 3D mesh mat and clay and demolition of paving stones.

when an erosion hole developed at the dike toe due to jet erosion, reaching the flume bottom (30 cm) (Fig. 7 k).

e) V5: with paving, curb stones, 3D mesh mat and rolled turf

The final vertical transition experiment, V5, including rolled turf, further increased the applied loading up to 382 min, reaching final discharges of approximately 250 l/(s*m). During the first 90 min, most of the flow passed over the smooth paved sides of the model, while the grass was gradually submerged. A fully deflected and submerged grass cover was reached after 155 min at approximately 34 l/(s*m). Since this flattening is not considered erosion in the evaluation of the 3D scans, test V5-S15 was defined as the initial state for the analysis (see Fig. 12). No visible damage occurred during the first 165 min up to a discharge of approximately 34 l/(s*m). Initial erosion was observed during the final 15-min test at 34 l/(s*m), beginning in the lower-slope area and progressing upstream in the course of testing. The first damage was considered a modelling effect, as erosion initiated at the sharp edges of the turf roll strips. Due to the limited growing period and non-uniform root development along the slope length, complete bonding between the turf strips and the underlying clay could not be ensured. This was especially evident near the dike toe, where the turf could be lifted easily, likely due to the damp conditions (see also Fig. 4). At approximately 68 l/(s*m), initial damage to the 3D mesh mat was observed in the lower slope area, occurring under a much higher loading than in V4. The turf, clay, and reinforcement layers were eroded successively with a slight offset. At higher discharges, however, the 3D mesh was detached together with the turf due to the root network within the mesh and the shear interface between the layers. The nonwoven textile effectively protected the transition areas against deep erosion and was only undercut near the dike toe. Compared to the previous experiment, no clear advantage of either installation method of the nonwoven textile and 3D mesh could be identified, although this may be influenced by differences in root penetration of the turf stripes through the nonwoven textile. It is therefore important to ensure that the nonwoven textile used allows for good root penetration ($<200\ g/m^2$). From approximately 96 l/(s*m), a scour hole developed behind the paved area at the dike toe due to jet erosion. The experiment was terminated when the scour hole reached the model bottom, and several paving stones near the crest were destabilized. Overall, V5 demonstrated a substantial increase in erosion resistance, withstanding more than twice the maximum loading compared to V4.

4.1.2. Horizontal transitions

The tests with horizontal material transitions show, overall, higher erosion than the reference case V1 or the vertical transitions. Erosion starts at the material transition but quickly spreads over a larger area in the direction of flow. Photographs of each horizontal test setup before and after testing, along with a color plot of the erosion depths after the final test, are shown in Fig. 13.

f) V6: with paving and curb stones

Test setup V6 failed after 65 min of operation at a maximum overflow discharge of approximately 10 l/(s*m). The experiment was terminated due to several critical failure mechanisms, including exposure of the downstream faces of the curb stones, undermining of the paving stones, and tilting of the curb stones (see Fig. 13 e). Initial erosion occurred directly at the joint from the curb stone to the downstream clay, forming a small vertical drop that intensified over time and resulted in an

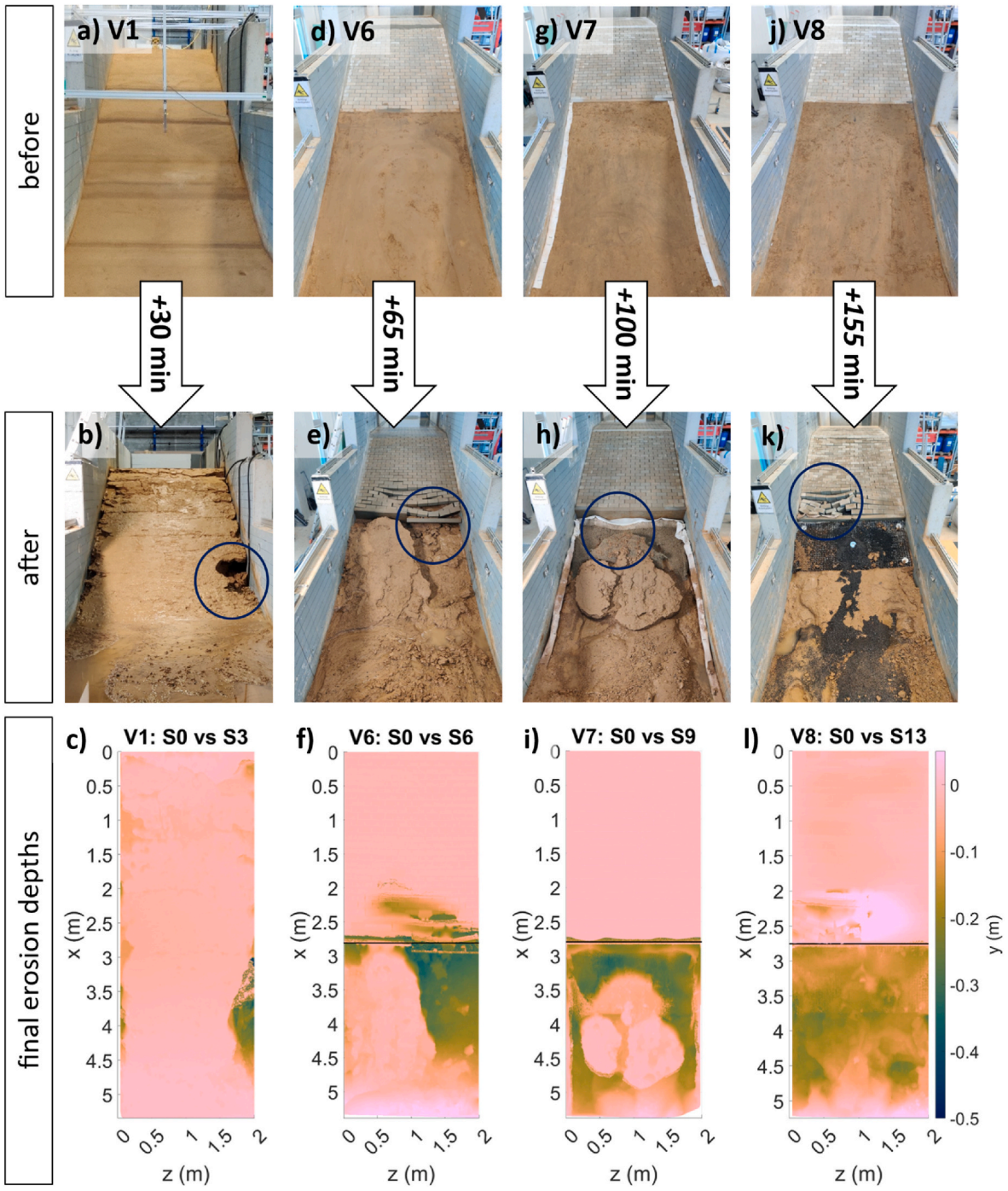


Fig. 13. Initial and final state before and after testing and difference plots of landward dike slope after final testing horizontal transition setups a)-c) V1, d)-f) V6, g)-i) V7, j)-l) V8 with the testing time for each configuration, the final experimental number S and indication of initial transition location; the circular markings indicate the location where the critical erosion depth as termination criteria was reached.

increasing erosion depth. The overflowing water continued to impact the slope, generating jet erosion downstream of the curb stones. During the second test (*S2*) at a lower discharge of roughly 5 l/(s*m), water already exited from the joints between paving stones approximately 30 cm upstream of the curb stones and directly at the curb stones, which gradually caused tilting of the curb stones and showed the development of additional subsurface flow below the paving stones. The flow concentrated on the right-hand side of the model, where it led to pronounced localized erosion (up to >0.3 m). The dry peninsula forming in the clay on the left-hand side downstream of the transition (see Fig. 14 b in dashed line box) was narrowed laterally, while overhanging sediment collapsed progressively.

After termination of the experiment, the paving stones were removed to quantify the extent of subsurface erosion. In total, a volume of ~0.176 m^3 was eroded beneath the paving stones over an area of ~1 m^2 (see Fig. 14 c).

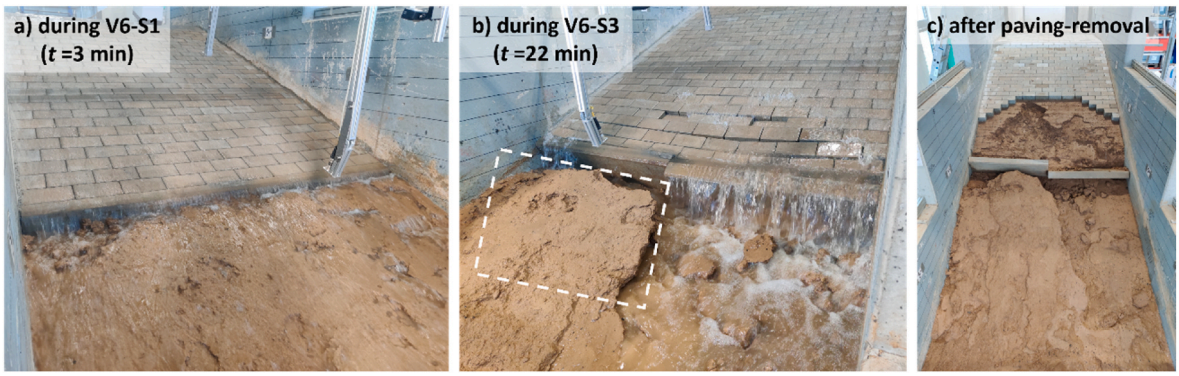


Fig. 14. Photographs during the experiments V6: a) first erosion close to material transition looking from downstream up the slope, b) water overfall over tilted curb board and sagging of paving stones looking from downstream up the slope; erosion depth at this state up to 0.27 m, c) overview of erosion under paving stones after final test.

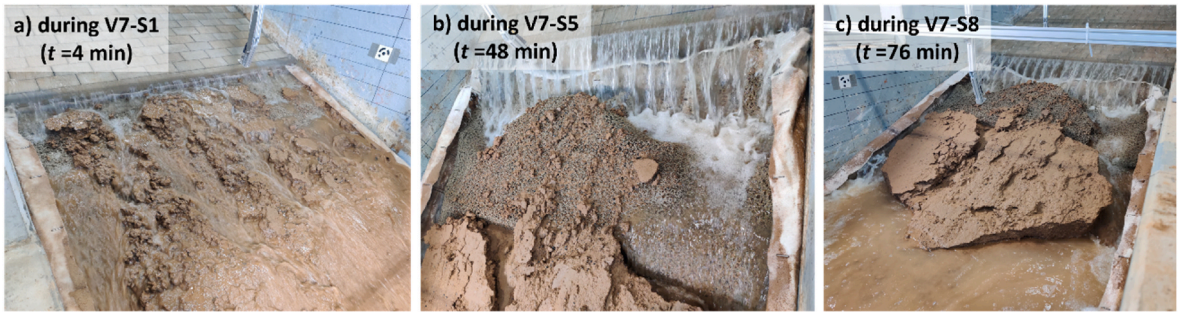


Fig. 15. Photographs during the experiments V7 looking from downstream up the slope: a) first erosion of clay topping on 3D mesh, b) water overfall over the edge formed by the curb stones, bulging of 3D mesh and erosion in embedment trench region, c) water overfall, separation of flow under 3D mesh and flow along flume walls.

g) V7: with paving, curb stones and biodegradable 3D mesh mat installed with embedment trench

With the implementation of a filter geotextile as well as 2 cm gravel bedding under the paving stones, the whole upper paved dike part was strengthened, and no washout or tilting of curb stones was observed in the experiments of V7. The lower part was reinforced by a 1-m stretch of a biodegradable 3D mesh mat, which led to a small increase in erosion resistance, but was still undermined and ripped. It was observed that the integrated mesh mat initially functioned as a sediment trap (Fig. 15 b), retaining eroded clay beneath the mat and bulging at the embedment trench; however, the mesh subsequently failed, and erosion progressed beneath the mat. Overall, the mesh mat didn't prevent the progression of erosion in depth within the jet-impact zone of the water overfalling the curb stones. Still, it adhered to the eroded surface, creating additional turbulence. The new exposed transition from the 3D mesh mat to the clay at the embedment trench also showed a high risk of erosion, and the previously compacted integration trench was quickly washed out. After 100 min with approximately 22 l/(s*m) (much lower loading than the V4 setup), the tests were terminated because the 30 cm erosion depth was reached due to exposure of the downstream faces of the curb stones (see Fig. 15). Furthermore, localized tearing of the mesh mat led to its loss of stability, and the non-woven geotextile was entirely washed away and no longer integrated into the clay, suggesting that the reinforcement measure did not achieve its intended function, although it showed better performance under vertical transitions (V4).

h) V8: with paving, curb stones and non-biodegradable anchored 3D mesh mat

Because the improvement of the clay area downstream of the transition was still not ultimate, an alternative material for the 3D mesh mat, along

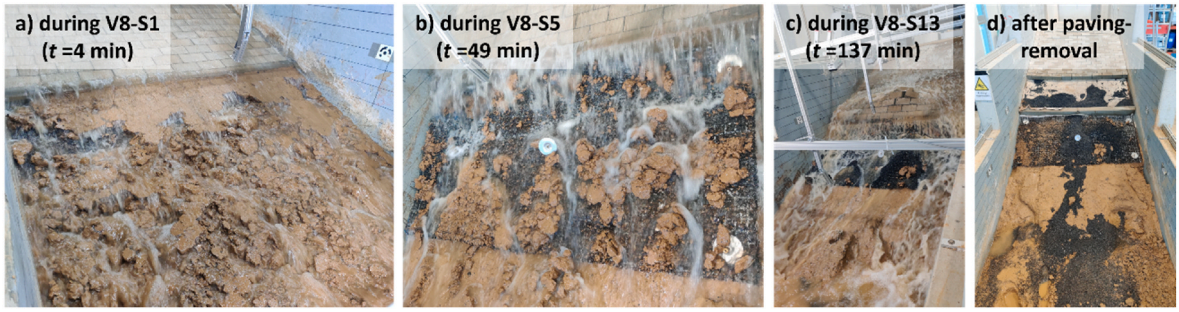


Fig. 16. Photographs during the experiments V8 looking from downstream up the slope: a) first erosion of clay topping on 3D mesh, b) water overfall over curb board, sagging and undercutting of the 3D mesh mat so that anchors are no longer tensioned, c) bulging of paving stones before collapse and termination of experiment, d) setup after removal of paving stones showing the washout of gravel bedding.

with another installation technique of the erosion control product, was selected for testing in V8. With the first load level and during the first 10 min of testing, most of the clay on top of the 3D mesh mat was already eroded as expected (Fig. 16 a). During further testing, clay beneath the mat was eroded, creating sub-mat erosion paths without any local maxima in erosion depth, and the anchors lost tension (Fig. 16 b). Despite this, the more robust mesh mat used (compared to V7) effectively resisted flow and turbulence without bulging, tearing, or bending. Although the underlying non-woven textile eventually sagged, the erosion control system remained functional and was not washed out. Until a discharge of ~22 l/(s*m), the paved area showed good performance without any noticeable subsidence or gravel washout. With the load increasing up to ~34 l/(s*m), the paving stones started to bulge (Fig. 16 c), vast amounts of gravel were washed out until it ultimately collapsed. This also marked the termination of the experiments, even though 30 cm of erosion depth was not reached (Fig. 13 k). Nevertheless, the mat did not fail, thereby improving the erosion resistance at the transition.

4.2. Analysis of vertical transitions

4.2.1. Erosion depth and volume

The erosion progress was quantified after each partial load for a constant discharge level or the cumulated overflow water volume (V_{cum}) for the soft and unpaved as well as total dike slope, respectively (Fig. 17 a).

In Fig. 17 a, it can be seen that erosion in reference test V1 progresses linearly. In test V2, the edge areas were reinforced with paving stones, which significantly reduced erosion on the model walls, which also represent a transition, and enabled them to withstand higher loads. Nevertheless, the total erosion volume across the entire slope is higher than if only the soft area is considered due to the failure in the paved areas (Fig. 7). Test V3 exhibits significant erosion, particularly after the initial load, but then proceeds at a comparable rate to test V2 during subsequent tests. The high initial erosion in V3 is due, in part, to the reconstruction of the test setup, as erosion was observed particularly in areas that were only repaired from V2 through small-scale repairs of the damage. Accordingly, the initial good compaction could not be restored, and erosion was initiated in the repaired areas. Comparing V2 and V4, one could clearly observe that the implementation of the 3D mesh mat below the clay layer resulted in similar erosion rates at low load cases, but once the erosion depth reached the mat, it significantly prolonged the time until the critical erosion depth criterion was reached. The test setups V4 and V5, enhanced by the 3D mesh, also exhibit fairly linear erosion patterns before the progression accelerates to the final failure criterion. In experiment V4, more than four times the loads of V3 could be resisted, whereas in V5 they were again doubled compared to V4. All setups show roughly 2 times higher erosion per unit area when considering only the soft area rather than the whole slope, except V2, highlighting the relatively strong influence of the soft area on erosion compared to the paved areas.

In Fig. 17 b, the overall maximum erosion depth ($d_{e,max}$) on the entire slope as well as the soft area alone over V_{cum} is displayed. Overlap of symbols for a specific setup indicates the location of the maximum erosion depth in the soft area. The maximum depth per setup shows quite a similar progression to the mean erosion depth as the erosion volume over area, except with an overall factor of ~10, highlighting local erosion maxima. Besides, oscillation in $d_{e,max}$ indicates the deposition of the eroded sediment from the upstream. The highest erosion

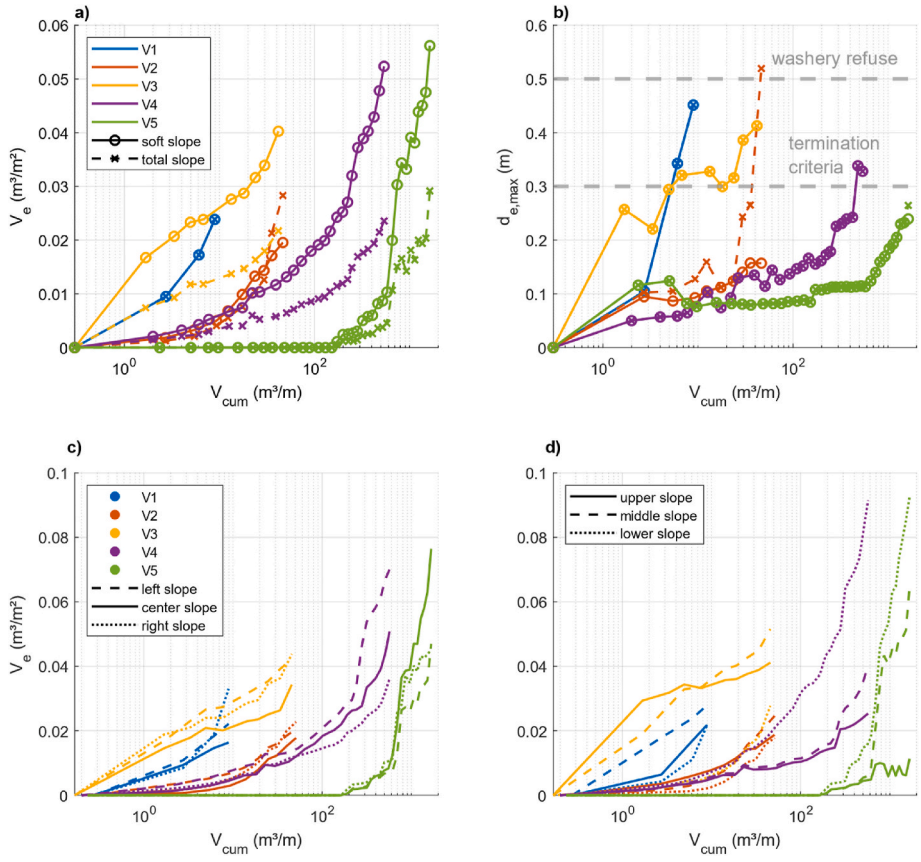


Fig. 17. a) Eroded volume per total soft dike area and per total dike slope area V_e, b) maximum erosion depth $d_{e,max}$ on slope for soft and total slope (Hint: for V5, $d_{e,max} \leq 0.08$ m is considered as the mean grass deflection), c) eroded volume per soft dike area V_e for subareas separated in vertical subareas of left, center and right slope (see Fig. 3) and d) eroded volume per soft dike area V_e for subareas separated in horizontal subareas of upper, middle and lower slope as a function of the cumulative overflow water volume per running dike meter V_{cum} for vertical transition setups.

depth in V2 is localized in the collapsed paved area. In V5, the deflection of grass blades is considered in the first 14 experiments, showing a mean grass deflection of ~8 cm. The results for $d_{e,max}$ in V4-V5 highlight a more gradual development of local erosion maxima due to the erosion control measures and proper substructure of paving.

By separating the unpaved (soft) slope area into subareas, additional characteristics can be derived (Fig. 17 c and d). For V1-V3, the edge areas (left and right) exhibit higher erosion volumes than the center part, indicating that, with a higher distance to the transition, a lower erosion volume. When reinforced with the 3D mesh mat, this trend shifts. In V4, the highest erosion volumes are found in the left subarea of the slope, followed by the center subarea, agreeing with visual observation. This result quantitatively demonstrates that the various approaches to reinforcing the transition are effective to varying degrees on the left and right sides of the slope. The right-side method, which involves wrapping the 3D mesh mat with nonwoven geotextile, provides higher erosion resistance than the method used on the left side and even the center section of the slope, which is protected only by the 3D mesh mat. In V5, it is evident that the erosion volumes in the center section are nearly twice those of the edge areas, showing that the transition tends to have no higher erosion potential anymore, but rather shifts the erosion zone away from the improvement measures (Fig. 17 c). When looking at the slope in the longitudinal direction, it can be seen that for V1-V3, the highest erosion occurs on the middle and upper slopes (Fig. 17 d). This erosion pattern can probably be attributed to the combination of the geometric slope transition at the inner crest line and the absence of erosion protection on the upper slope. The change in slope geometry can locally intensify the flow and promote erosion initiation, while the lack of protection allows this initial erosion to develop further. Once local damage has formed, flow concentration can further accelerate erosion and promote its progression on the upper and middle slopes before the flow reaches the lower slope, eventually resulting in failure of the upper and middle slopes. During the experiments of Scheres and Schüttrumpf (2020) with a grass-herb mixture, similar erosion patterns were observed, with the middle slope being eroded the most. For tests V4-V5, the highest erosion volumes are analyzed on the lower slopes. This can be explained by the higher strength of the areal reinforced clay surfaces, leading to a shift in rapid erosion development towards the lower slope, where flow velocities and cumulative overload are also highest and jet impact is a governing failure mechanism (Hoffmans et al., 2013). Due to the protective function of the 3D mesh mat against erosion, mostly particle erosion is initiated and block erosion is hindered by the enhanced shear strength of the erosion control system (Pan et al., 2015).

4.2.2. *Spatial erosion patterns*

The mean erosion depths over the slope length in the along-dike cross section for the different experiment setups and the cumulative overflow volume on a log color scale are shown in Fig. 18 to indicate the spatial

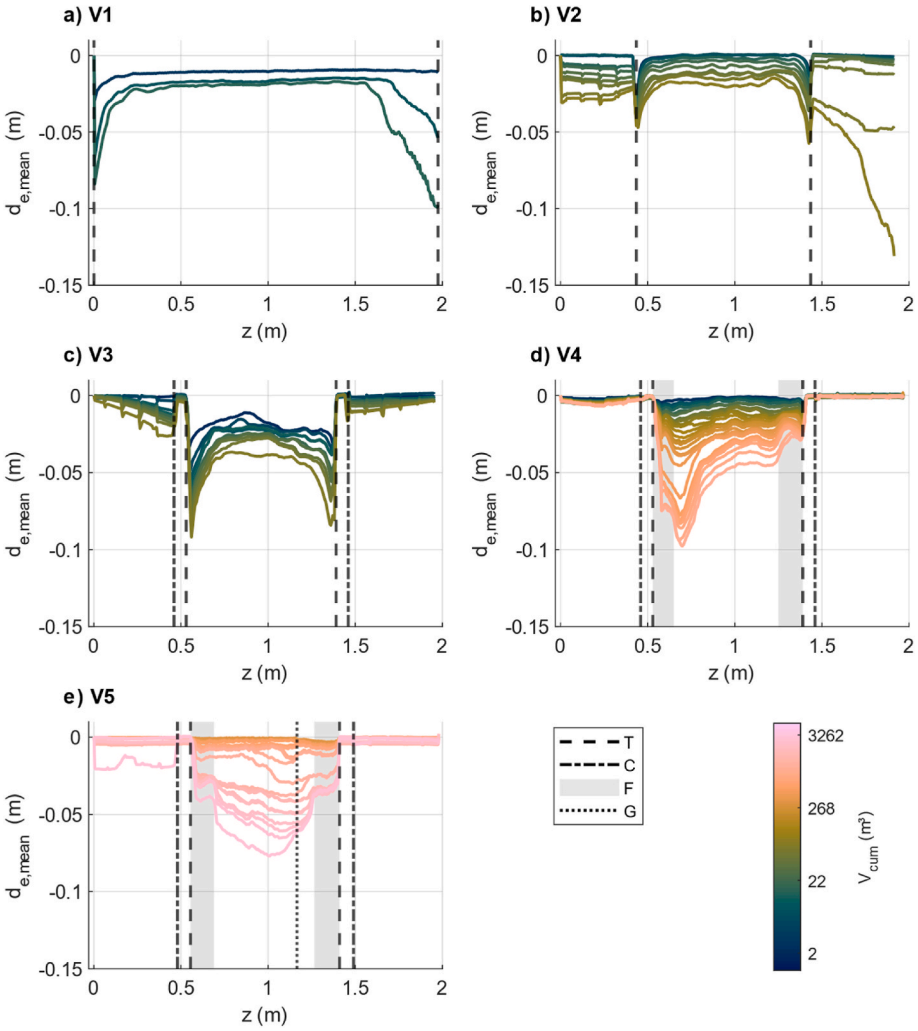


Fig. 18. Mean erosion depth $_{de,mean}$ (negatively annotated) as a function of the dike width z for: a) V1, b) V2, c) V3, d) V4 and e) V5, with the cumulative overflow volume on erosion development after repeated exposure in logarithmic scale color gradient and lines/areas indicating T: transition from hard to soft, C: curb stone, F: non-woven fabric and G: turf roll edge. (For interpretation of the references to color in this figure legend, the reader is referred to the Web version of this article.)

erosion patterns. As with the visual observation, increased erosion occurs in the wall areas and at transitions from hard to soft surfaces for V1-V3, before gradually decreasing with increasing distance to the hard material change. For V4, it can be observed that erosion in the transition areas is inhibited by the geotextile nonwoven textile (transparent grey-filled area). The textile is placed initially 5 cm below the dike surface, indicating that on the left side of the slope, on average, the erosion is also undercutting the textile slightly, while on the right side, the erosion protection products (3D mesh mat and non-woven textile) are, on average, not even reached by the erosion. However, the erosion progression is slower in the areas of the textile or the 3D mesh mat, but is accelerated once the protection by the textile and mat is removed, which is seen especially for the left side of the slope (Fig. 11 d and Fig. 18 d). With the assumption of the initial state for the evaluation of V5 once the grass is fully deflected (after V5-*S*15), a relatively uniform erosion progression over the flume width can be observed. The protection of the transition areas due to the non-woven textile can be seen again, as well as the cut edges of the turf rolls. An overall improvement in the settlement and undercutting of the paving foundation can be found by including the stones directly into the clay (V4-V5).

4.2.3. *Erosion rate and hydraulic loads*

The erosion rate E_i over the soft area, per test campaigns and over the different load levels, is evaluated in Fig. 19. With each new connected line in plots a) to e), the erosion rates normalized to the erodible area are shown per test and per mean discharge. The figure illustrates the extent to which the erosion rate increases with flow rate and whether there are differences at the same flow rate. Fig. 19 f then shows the mean and maximum erosion rates per load level in order to highlight the erosion progress between the different test setups.

The overall erosion progression per test campaign and over the different load levels is relatively constant, with erosion rates ranging between $0 < E < 16$ cm^3/(s*m^2) for discharges $q_w < 100$ l/(s*m) (Fig. 19). One exception is the first test campaign of V3, where high initial erosion was observed with an erosion rate up to 28 cm^3/(s*m^2). For V5 and higher discharges $q_w > 100$ l/(s*m), more unusual erosion progress can be observed. Both very high initial erosion with a higher discharge level $E > 24$ cm^3/(s*m^2) and negative erosion progression can be seen. This can be explained by the position of the washed-out geotextile at the toe of the dike during the scanning process, which covered eroded areas. While lower discharges were associated with persistently low and stable erosion rates, increasing the discharge to 170-210 l/(s*m) resulted in abrupt but non-systematic peaks in erosion exceeding $E > 10$ cm^3/(s*m^2). However, it is notable that elevated erosion rates were consistently observed primarily at the beginning of a new discharge level, usually within the first or second loading cycle, and diminished with further loading.

Fig. 19 f shows the mean and maximum erosion rates as a function of discharge. Overall, erosion rates increased with increasing discharge, although some local decreases were observed. Protection measures generally reduced erosion rates compared with the unprotected configurations, except for V3, where local repairs affected the results. It should be noted that these erosion rates were determined for the entire clay-covered slope, including areas influenced by hard-material transitions, which locally increased erosion. Therefore, they do not represent erosion rates of a homogeneous clay slope without transitions. To assess

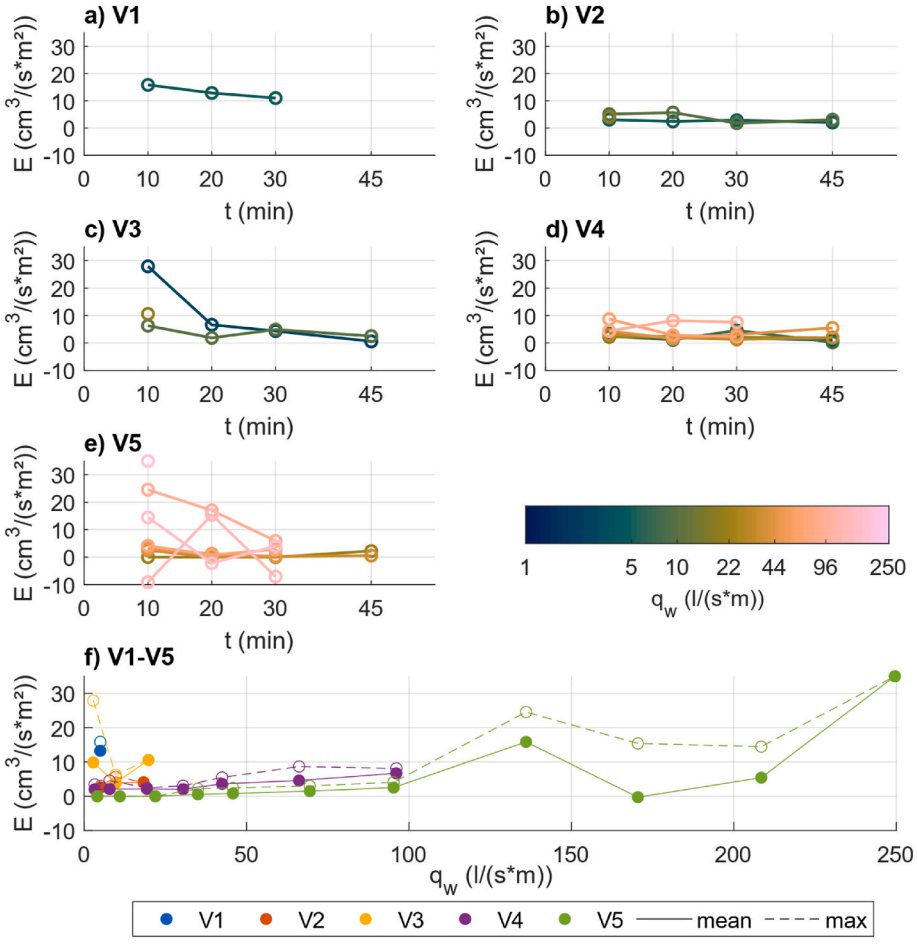


Fig. 19. Erosion rate E (cm^3/s) per soft area (m^2) as a function of time and load level (discharge q_w) for the different experiment configurations: a) V1, b) V2, c) V3, d) V4, e) V5 and f) mean and max erosion rate E of different test campaigns per load level (discharge q_w) for different experiment configurations.

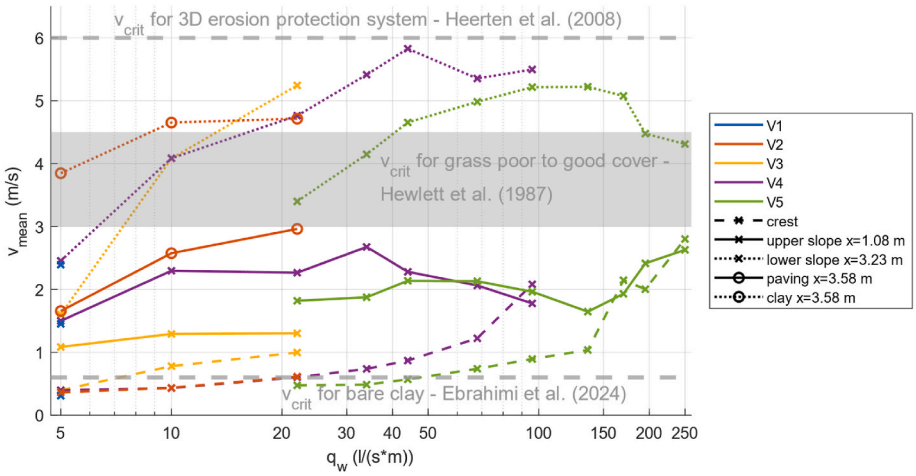


Fig. 20. Measured mean surface velocity v_{mean} of individual tests of the same discharge level over the mean discharge q_w (log-scale) for different experiments with vertical transition and sensor positions. Critical velocity v_{crit} limits from literature show initiation of erosion for different materials.

erosion unaffected by transitions or wall effects, the central 1 m of the slope in V1 was evaluated separately. The resulting mean erosion rate of 10.45 $cm^3/(s*m^2)$ exceeded those of the transition configurations, indicating that initial erosion was dominated by removal of the surface layer rather than by the presence or absence of transitions.

In Fig. 20, the measured mean surface velocities from the surface radars for the steady flow duration and the individual tests at each discharge level are plotted against the discharge. It can be seen that the surface velocity at all measuring positions increases overall with higher discharge up to a discharge of 34 l/(s*m). After that, velocities on the crest tend to rise further, while the velocities measured on the slope for V4 and V5 show some fluctuations, most likely resulting from progressive erosion and surface irregularities, which can increase roughness and therefore decelerate the flow. In addition, an increased surface velocity can be observed with increasing distance from the crest, as expected. For V2, it can be deduced that the velocities not only differ longitudinally, but also tangentially, and that higher velocities are measured on the middle clay area due to lower roughness. Test V5 with turf also shows that for the initial discharges, when the turf was still intact, lower velocities are achieved on the slope with increased roughness. Since the turf was not fully deflected and submerged at all locations for discharges below 20 l/(s*m), the measurements cannot be considered fully reliable in this range; therefore, only data above this threshold are presented. Further initial critical velocity limits from the literature indicate the erosion initiation of bare clay (Ebrahimi et al., 2025), grass (Hewlett et al., 1987), and geosynthetics and grass cover (Heerten et al., 2008). These critical velocities are consistent with the observed damage patterns; however, it should be noted that the transitions lead to additional erosion, the flow field is three-dimensional, and the material properties of the soil and the embedded materials may differ significantly from those reported in the literature.

4.3. Analysis of horizontal transitions

4.3.1. Erosion depth and volume

For the horizontal transitions V6-V8, the lower dike part ($x > 2.87$ m) represents the soft area of the slope, while the upper part is paved. Fig. 21 shows the erosion volume per area of the total and soft dike slope as well as the maximum erosion depth as a function of the cumulative overflow water volume V_{cum}. Overall, the horizontal transition setups

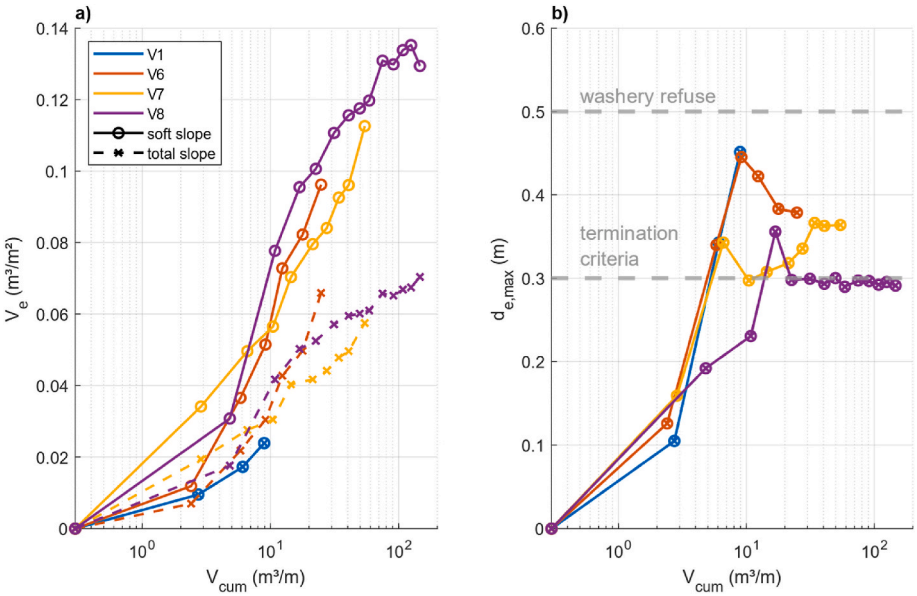


Fig. 21. a) Eroded volume per total soft dike area and per total dike slope area V_e and b) maximum erosion depth $d_{e,max}$ for soft and total slope as a function of the cumulative overflow water volume per running dike meter V_{cum} for horizontal transition setups.

exhibit higher erosion volumes than the reference test, indicating a greater erosion risk of disrupting material and soil structures. The sudden change in material triggers erosion and increases the erosion depth in the vicinity of the curb stones, and water impacts on the soil downstream.

Comparing the erosion volumes V_e and erosion depths $d_{e,max}$ in Fig. 21 against V1, V6 show comparable erosion behavior in the first test *S*1 (i.e., during the initiation of overflow, but subsequently exhibits greater erosion volumes. Comparing V7 with V6, it is seen that at lower load levels, the erosion is higher, but then slows down a bit after the clay layer up to the top of the 3D mesh mat was eroded. This demonstrates the effect of the erosion-control measure, which becomes effective after exposure and can withstand higher loads overall. In V8, the initial overall erosion progression was comparable to that in the V6 experiment. Nevertheless, after reaching a mean erosion depth of 0.1 m, the tests were continued, and the erosion ultimately reached a plateau starting with a discharge of ~22 l/(s*m). Negative slope gradients in the graph resulting from the last test indicate gravel deposition from the paving bedding on the lower slope. As for the erosion depth, the decrease in maximum erosion depths in sections V6-V8 is likely due to the accumulation of eroded material (see Fig. 21 b). While for V6-V7 the maximum erosion depth is identified directly downstream of the curb stone, it is shifted to the transition of the 3D mesh mat to soft material at the wall in V8. Overall, the graph indicates that an equilibrium was reached in the V8 experiment, with no locations having a maximum erosion depth of greater than 30 cm. Still, failure of the paved area due to gravel accumulation in the lower paved area, leading to subsurface flow accumulation on the filter geotextile and, ultimately, collapse due to the breaking of interlocking paving stones, was observed.

Although the total erosion volume for V8 was higher than in all other tests, its visual performance was the most favorable (see Fig. 16), highlighting the importance of considering not only total volumes but also maximum erosion depths (Fig. 21 b). In V6 and V7, model- and wall-related effects led to increased erosion along the flume walls (Fig. 13), creating deeper flow channels and leaving large areas downstream of the transition relatively unaffected. In contrast, the distribution of maximum erosion depths indicates that, while V1, V6, and V7 exhibited similar patterns up to a cumulative overflow water volume of ~7 m^3/m, V8 achieved a significant reduction in maximum erosion depths, with up to 15 cm difference.

4.3.2. *Spatial erosion patterns*

In Fig. 22, the mean erosion depth over the dike width is shown for the cross-dike slope length and different experimental setups as well as loads, with $x = 0$ m denoting the transition from dike crest to slope and $x = 5.4$ m indicating the downstream end of the slope at the dike toe. In the horizontal transition test, the material changes are weak points, exhibiting the highest erosion. The highest erosion depths are observed immediately downstream of the transition and, overall, decrease with increasing distance from the transition, ending with a mean clay deposition at the downstream end of the slope. For V7, three localized erosions are evident: increased erosion in the 3D mesh mat area, increased erosion within the binding trench of the 3D mesh mat, and increased erosion at the dike toe. The pronounced erosion in the embedment trenches demonstrates that localized soil disturbances, created when trenches are excavated after layered compaction, are highly susceptible to erosion. Such areas require either avoidance during curb stone or geotextile installation, or meticulous recompaction to ensure stability. In addition, the first test showed that erosion had already increased significantly up to the height of the 3D mesh mat. In V8, erosion progresses more evenly, and the highest erosion is not observed at the transition from the curb board to the 3D mesh, but rather at the transition from the 3D mesh mat to the unprotected clay on the lower dike slope. In both V7 and V8, it is evident that the implementation of the 3D mesh mat became effective as soon as the upper clay layer was eroded and then erosion subsequently progressed more slowly, even though the mesh mats were also undermined and settled. In V8, in particular, a stagnation in erosion depth is observed at ~0.13-0.17 m from the original dike surface. In addition to the aforementioned transitions from curb stones to 3D mesh mat and from 3D mesh mat to clay, the end of the

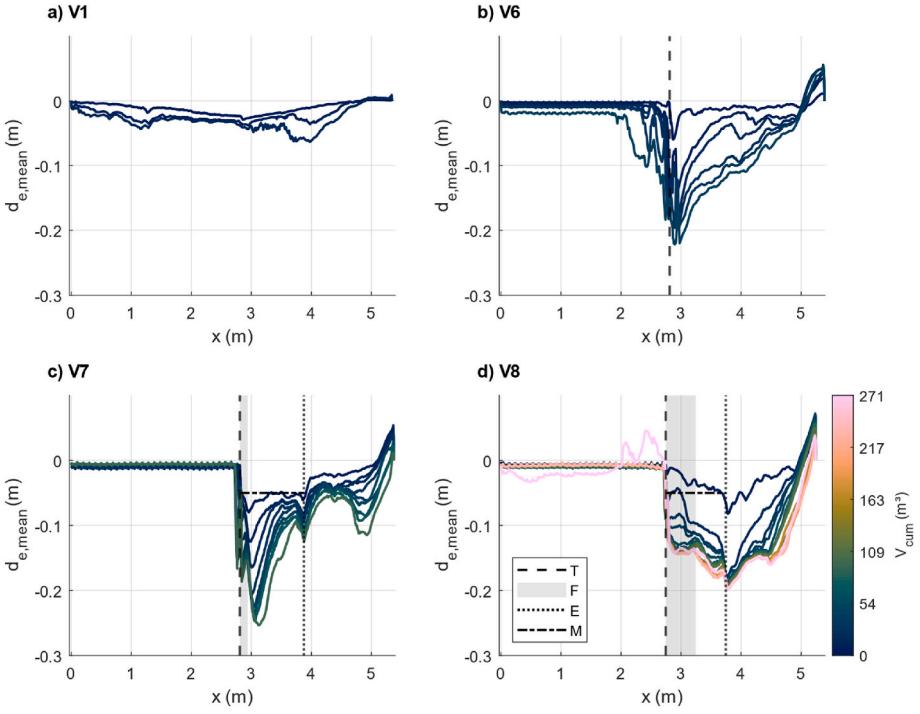


Fig. 22. Mean erosion depth $_{de,mean}$ (negatively annotated) as a function of the dike length *x* for: a) V1, b) V6, c) V7, d) V8 with partial load on erosion development after repeated exposure in color gradient and lines/areas indicating T: transition from hard to soft, F: non-woven fabric, E: embedment trench respectively at the end of 3D mesh and M: initial installation depth of 3D mesh mat. (For interpretation of the references to color in this figure legend, the reader is referred to the Web version of this article.)

non-woven fabric under the 3D mesh is also visible in V8 ($x = 2.87$-3.37 m). The area covered by the non-woven fabric shows overall slower erosion progression than the part only secured by the 3D mesh mat due to shielding. While the fabric is also undermined and settles to an average of 10 cm below its initial position, it continues to protect the underlying soil from further erosion. As no additional erosion progression is observed with increasing loading, the erosion depth stabilizes at a medium depth of ~15 cm. An overall improvement of the settlement and undercutting of the paved areas through a filter layer under the paving stones could be achieved, which is seen when comparing V6 with V7-V8.

4.3.3. Erosion rate and hydraulic loads

The erosion rate E_i ($cm^3/(s*m^2)$), as defined in section 3.3, is presented in Fig. 23. For horizontal transitions, the maximum erosion rates are nearly three times higher than those observed for vertical transitions, with $E > 85$ $cm^3/(s*m^2)$. Notably, in V7 and V8, elevated erosion rates occurred predominantly at the lowest flow rates, corresponding to the initial load. This behavior can be attributed to the erosion of the clay above the 3D mesh mats before the mats are able to effectively mitigate further erosion. In contrast to experiments with vertical transitions, erosion rates tend to decrease with increasing flow rates (Fig. 23 e), suggesting that a quasi-equilibrium state in erosion development is reached.

Measured average surface velocities for the duration of the steady flow and the individual tests at each discharge level are plotted against the mean discharge in Fig. 24. Since the crest was completely paved in the tests with horizontal transition, the velocity distribution on the crest

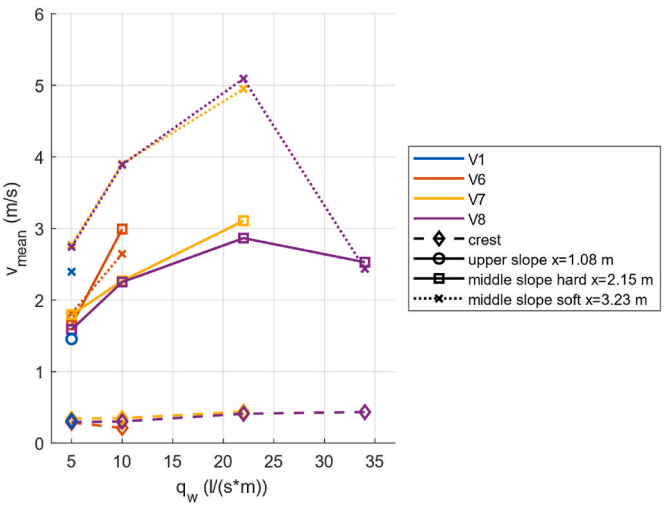


Fig. 24. Measured mean surface velocity v_{mean} of individual tests of the same discharge level over the mean discharge q_w for different experiments with horizontal transition and sensor positions.

is also comparable across the setups, with an average velocity of ~0.4 m/s. It can also be seen that the velocity overall increases with greater distance from the crest (exception V6). For V8, it appears that for the largest discharge of approx. 34 l/(s*m), there was a reduction in the velocity data compared to the flow rates before. This can be attributed to

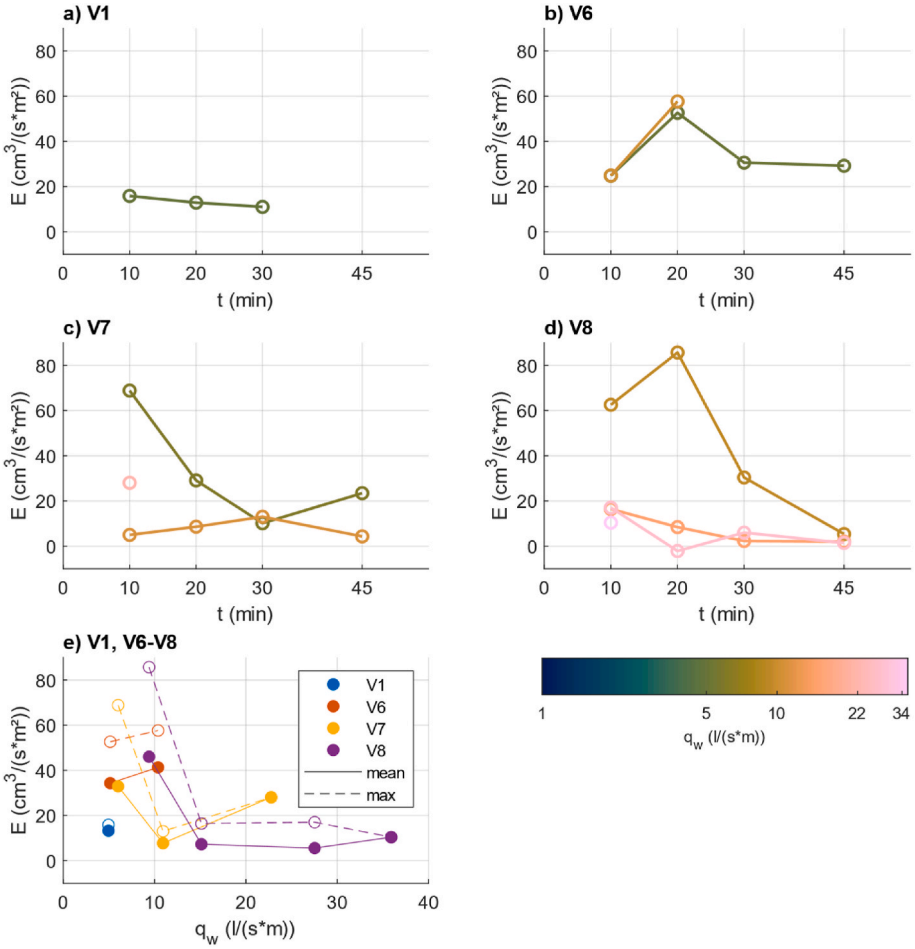


Fig. 23. Erosion rate E (cm^3/s) per soft area (m^2) as a function of time and load level (discharge $_{qw}$) for the different experiment configurations: a) V1, b) V6, c) V7, d) V8, e) mean and max erosion rate E of different test campaigns per load level (discharge q_w) for different experiment configurations.

the final test of V8, during which the paving stones bulged, flow was significantly diverted, and an abrupt failure occurred. The resulting highly uneven flow patterns suggest that point measurements under these conditions cannot provide fully accurate results.

5. Discussion

Previous large-scale experiments have provided quantitative data on erosion volumes, particularly for seaward dike slopes subjected to wave impact (van Bergeijk et al., 2025). For landward dike slopes, however, quantitative information on erosion volume and its temporal progression remains limited, particularly for slopes containing geometric or material transitions. The present study quantified erosion volume, erosion depth, and erosion rate as a function of cumulative overflow volume. The experiments were conducted under the same soil and hydraulic conditions and evaluated relative to a reference test, allowing the influence of the investigated transitions on erosion development to be assessed and helping to inform appropriate dike reinforcement measures. Most importantly, the tests with both vertical and horizontal transitions showed that the transition strongly influenced the initiation of erosion. Many erosion processes are associated with transitions and changes in the local flow characteristics. Due to the implementation of erosion control measures in transition areas, a shift, equalization, or even reduction of erosion was observed, which shows high potential for improving transitions. From the quantitative results of erosion volumes, depths, and rates, it can be seen that horizontal transitions are more vulnerable than vertical transitions. Nevertheless, due to model effects, erosion along the walls (V1 and V6-V7 as erosion along buildings in reality within the dike structure) also shows high erosional potential, which could be mitigated by a properly constructed paved area along these walls.

A direct comparison of the present study results of time-resolved or hydraulic loading-based erosion volumes is not feasible due to data limitations. Hence, Fig. 25 compares other studies on wave overtopping and overflow experiments on landward dike slopes with the V5 experiment of the present study based on the total test duration t and the cumulative overflow water volume V_{cum}. This comparison is not the primary focus, but is intended to provide context regarding the range and magnitude of conditions tested in other investigations, including different materials and dike slopes, thereby illustrating the wide range of parameters that influence erosion behavior. It further highlights that erosion tests are highly parameter-dependent and case-specific, whereas the experiments presented here constitute systematic tests designed to demonstrate the potential for improving transitions while remaining consistent with previously reported loading conditions. Most studies test few discharge levels over extended periods, showing linear paths rather than gradual increases. The additional influence of many incoming and outgoing waves can be minimal in these long, steady overflow cases, but progressive erosion information is missing without intermediate breaks for surface recordings. Some studies report greater erosive power coming from a wave front rather than continuous overflow (van der Meer et al., 2010a). Overall, the tested discharges in the present study are rather small, with a slower, gradual increase in load compared to other experiments. Some tests even show overflow durations up to 24 h over vegetated dike sections, which are not included in the figure due to clarity (Thornton et al., 2014). Experiments with bare clay material covers are obviously more sensitive to erosion and are therefore failing earlier. The effects of transitions and slope angle (Born et al., 2025) also influence the time of failure, while other experiments, such as Scheres and Schüttrumpf (2020), show only minor failures or no failure after the end of the experiment. It is estimated that the strength of grass is about 100 times greater than the strength of clay revetments (Hoffmans, 2012). Even though the grass revetment in V5 is affected by vertical transitions and is therefore expected to be weaker than a continuous revetment, and the clayey silt in V1 is influenced by wall effects, the results of this study demonstrate that the applied hydraulic loading in V5 could be increased by a factor of 50 and the overflow duration by a factor of 13 compared to V1. A direct comparison of steady overflow experiments with naturally occurring unsteady overtopping wave loads is not possible (Pan et al., 2015; Scheres and Schüttrumpf, 2020; van der Meer et al., 2010a). Previous investigations show that, despite equal shear stress existing for overtopping and overflow, the damage to the cover layer was more serious for wave overtopping, considering the significant influence of normal stress resulting from separation of flow and reattachment on the landward slope (van Damme et al., 2016).

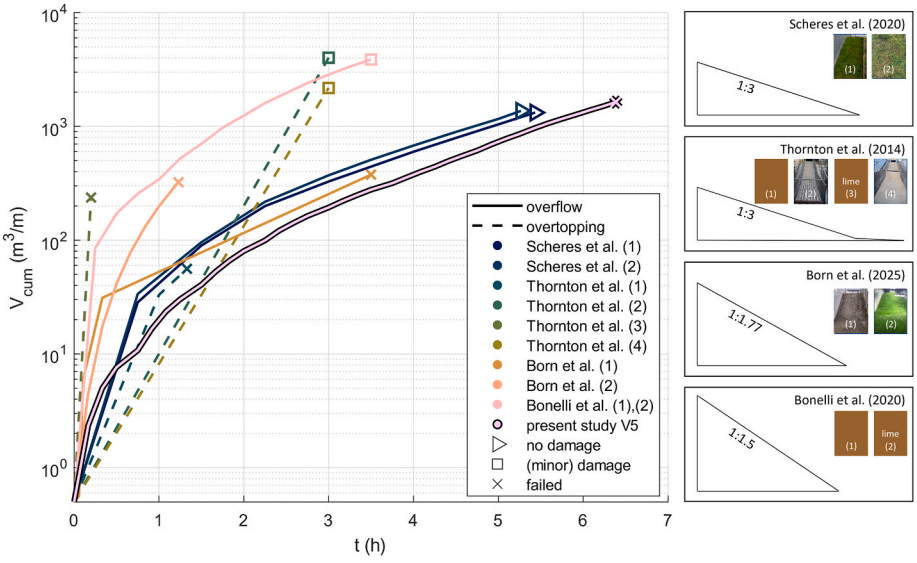


Fig. 25. Cumulative overflow volume V_{cum} over testing time t for different overflow/overtopping tests from literature, indicating the tested loads, landward dike surface materials, slope angles, as well as the final state of damage. (Scheres and Schüttrumpf, 2020): (1) TV1 - species-poor grass-dominated mixture, (2) TV4grid - grass-herb mixture with geogrid reinforcement; (Thornton et al., 2014): (1) bare clay, (2) articulated concrete blocks (ACB) on clay, (3) lime-stabilized clay, (4) dormant bermuda; (Born et al., 2025): (1) washery refuse, (2) grass Emscher mixture; (Bonelli et al., 2018): (1) untreated cohesive soil, (2) lime-treated soil.

5.1. Recommendations for the practical application

The systematic model variations in the present study help develop transition construction recommendations applicable to landward dike slopes. Some findings confirm practical experience (EAK, 2007) lacking formal validation; others introduce novel methods for strengthening the transition area. Recommendations vary for vertical and horizontal transitions. For vertical transitions, strengthening includes curb stones along the hard surface and toe protection against sliding of paved areas. A 3D mesh mat improves erosion resistance for the soft surface (Pan et al., 2015) when installed along the curb stones and coated with a non-woven fabric. For horizontal transitions, framing of the paved area with curb boards and concrete backing is also advised so that the cascading effect of paving stones sliding and the subsequent increase in erosion can be averted (as was observed in V6). Here, only the non-woven fabric should be embedded along the curb stones, with the 3D mesh on top. Design should consider jet impact and scouring (Peeters et al., 2013; Verheij et al., 2012), suggesting larger areas with non-woven geotextile as well as appropriate fastening on the slope to control erosion deepening.

Material choice for erosion control is crucial. Tests comparing two erosion control products showed that synthetic PP had better resistance than biodegradable fibre mats, which tend to tear and degrade over time, especially under horizontal transitions due to water jet impacts. Biodegradable mats help initially establish sward on dikes, while synthetic materials offer greater durability but pose environmental concerns, limiting their use as surface layer protection in dike construction until today (Chu et al., 2012; Werth et al., 2011), even though they are technical structures (Heerten and Vollmert, 2013).

In general, transitions should be avoided whenever possible (Schulte et al., 2024). Any additional materials added to the structure can create additional weak spots. Above all, besides considerate planning of transitions, construction of transitions is a major criterion to consider, since local repair, embedment of geobuilding materials into the soil, shrinkage, and compaction were identified as erosion triggers. Damaged areas should therefore be rehabilitated over sufficiently large areas and compacted in appropriate layer thicknesses to restore the original structural integrity. When constructing transitions within dike slopes, particular care must be taken to ensure adequate compaction (Ebrahimi et al., 2025) of excavated and backfilled zones (Olschewski et al., 2015). Excavations and embedment trenches for both rigid structures (i.e., curb stones) and flexible geosynthetic materials (i.e., 3D mesh mat) are inherent weak points with respect to erosion initiation and should be protected by filter geotextiles. Integrating planning, construction, and maintenance measures holistically appears essential to achieving resilient and durable coastal infrastructure.

5.2. Limitations of study

A terrestrial laser scanner was used to intermittently capture morphological changes in this study. This approach performed well on flat, mostly unvegetated surfaces. However, erosion beneath reinforcement measures, such as 3D mesh mats, nonwoven geotextiles, or paving stones, could not be accurately captured, most likely resulting in an underestimation of the overall erosion analysis, which was also observed, e.g., in dune erosion analysis (Mehrtens et al., 2025). Other spatial measurement techniques, such as photogrammetry (Ebrahimi et al., 2025) or a pin-profiler (Olschewski et al., 2015) also have limitations. Photogrammetry can't capture shaded, reflected, or inaccessible areas, while pin profiler provide measurements only at discrete points, highlighting the need for a more sophisticated measurement device to achieve highly accurate identification of erosion volumes. To mitigate the inaccuracies, scans were repeated after removing supplementary materials like paving stones at locations showing significant erosion after the last test for each setup (done for V3, V6, V8). Additional limitations in the erosion volume magnitudes include undetectable washed-out cavities in the dike subsoil or erosion break-off edges that could not be detected due to unfavorable scanning angles, which may introduce further uncertainties into the analysis. For test V5, which featured a rolled turf revetment, the pre-scan for the analysis was chosen after the grass had fully deflected and submerged, but before visible damage occurred. This ensured that erosion volumes were not overestimated due to the grass height or the altered position of grass blades from previous experimental runs. Until experiment V5-S15, the grass only flattened, which was not considered erosion, and therefore represented the true initial state for 3D scan evaluation.

In the present study, a full-scale (1:1) cut-out model of a crest and upper dike slope was constructed using real materials. For real-world scenarios, particularly in areas with complex transitions and heterogeneous construction, small- to medium-scale tests may not be suitable due to scaling limitations (Pan et al., 2015). Some limitations related to the grass cover and soil properties should be noted. In the test with rolled turf, the roots had only grown for seven weeks and were therefore still very fine and weak. It is well documented that the stabilizing effect of a grass layer is strongly dependent on root development and quality (Piontkowitz et al., 2009; TAW, 1998; Hiller, 1989; Igwe et al., 2017; Vannoppen et al., 2016), an immature or damaged turf may exhibit significantly lower erosion resistance (Scheres and Schüttrumpf, 2020). The erosion resistance of the dike cover is primarily determined by the upper approximately 20 cm of the topsoil (van Bergeijk et al., 2021), where the dense root system of the vegetation enhances erosion resistance (Baets et al., 2006). It decreases in the underlying, less-rooted subsoil layers and is mainly governed by the quality of the clay. Root density or root length density over depth was not tested for the present V5 setup, as no additional disturbance points should weaken the turf through sampling with the probe. The surfaces without vegetation tested in this study were chosen primarily to understand the erosion initiation and resistance of the soil material itself in the vicinity of transitions. Consequently, the results may differ from those obtained with a fully developed turf layer, highlighting the necessity of considering turf condition in practical dike inspections and in the assessment of transitions. However, the case without turf still provides a more conservative estimate of the dike's resistance capacity at transitions, and hence it has been chosen as the reference test case. Further, considering the erosion control products used, especially the 3D mesh mat, it is worth noting that the full effect of the measure is only reached when applying a vegetation layer, where soil is locked, and roots can grow within the 3D mesh and form a compound (Pan et al., 2015).

The clayey silt used in the experiments, even though considered as conditionally suitable within the German guidelines for sea dike construction (EAK, 2007), may differ in texture, composition, and mechanical properties from classical coastal clay, limiting the direct transferability of results (Achmus et al., 2019). Erosion patterns were highly sensitive to construction details and soil handling; although the dike was built consistently by the same team, results remained strongly dependent on the specific soil and construction method. The shrinkage cracks observed in V1, e.g., may have formed earlier due to relatively low initial water content of the clay, likely caused by storage and handling under laboratory conditions with reduced humidity. As previous investigations have shown, soil integrity (no animal burrows, good compaction) is a key parameter that enables dike stability and higher resistance to erosion (Depreiter et al., 2025; Ebrahimi et al., 2025; Briaud et al., 2008). Consequently, the presented results primarily allow for a relative comparison between the investigated experimental setups, while their direct applicability to full-scale coastal dikes is constrained by the site-specific nature of soil properties, construction details, and environmental conditions.

Additional model effects should be considered. Edge effects, for instance, from the alignment of rolled turf strips, cable ducts, or glued curb boards at the model walls, may influence local erosion patterns (Mulahasan et al., 2021). The consideration of only the landward dike slope is also an assumption, supposing that possible dike failure on the

seaward side of a dike did not occur beforehand, nor influence the landward processes. Further model effects may arise from sidewall and boundary effects inherent to hydraulic flume experiments (Falkenrich et al., 2021), as well as from modification of bed shear stress (Guo, 2015), erosion and flow structure at the flume walls or laboratory construction limitations. Pinettes et al. (2025) implemented a notch in the middle of the dike crest to overcome this model and side effects related to increased erosion, and observed lateral erosion development on the slope. Such over-profiling of the soil structure can also serve as a preventive strategy to divert water away from transitions (e.g., over-profiling stairs). Layer erosion in clay was observed to be non-linear due to the clay's physical properties, often occurring suddenly rather than gradually, highlighting the complex failure mechanisms and three-dimensional flow patterns that may not be captured in simplified laboratory models and the instrumentation used.

Further, the vertical test series V1–V3 failed primarily at the middle and upper slope due to scour, undermining of paving, head cut, and collapse. However, the reinforced configurations V4-V5 showed that the onset of erosion was shifted towards the toe of the horizontal berm. This demonstrates that the 3D mesh mat effectively delayed erosion. However, the final failure states of V4 and V5 cannot be assessed conclusively, as these tests were terminated due to jet impact and scour at the dike slope toe, which are attributed to another geometric (and horizontal) transition. This suggests that the reinforced configurations may have withstood even higher hydraulic loads if toe scour had not governed the failure. For the horizontal transitions, the main failure mechanism was also jet impact, resulting from the drop in height at the transition from hard to soft material. Additional failure at the horizontal transitions was pronounced due to model effects, which cannot be avoided in the laboratory scale experiments.

6. Conclusion

Transitions were identified as erosion-prone zones characterized by locally reduced material strength (e.g., compaction variability) and locally intensified hydraulic loading, including increased flow velocities, shear stresses, turbulence, and concentrated flow paths.

The experiments demonstrate that the largest erosion depths and volumes consistently occur directly within the material transition, confirming its role as a primary location for failure initiation. Distinct damage processes were observed depending on transition type. Vertical transitions were mainly affected by soil–structure interface erosion, gully formation, and toe scour, whereas horizontal transitions were dominated by jet-induced erosion and collapse. Erosion rates were generally highest during the start of each new loading level (the first ~20 min of overflow), while repeated application of the same loading resulted mostly in a decrease of erosion rates. This suggests that changes in hydraulic forcing, rather than prolonged exposure to a constant load, were the main driver for increased erosion rates.

Quantitative analysis demonstrates clear differences between configurations, with horizontal transitions exhibiting overall erosion rates up to three times higher and greater susceptibility to failure compared to vertical transitions. For vertical transitions, erosion rates tended to increase with higher discharge, whereas the erosion rate decreased for horizontal configurations since significant erosion already occurred at lower discharge. Since all experiments were continued until failure (here: erosion depth of 30 cm), the final loading condition and the associated damage state indicate an estimate of the hydraulic load level that each dike configuration could withstand under the tested boundary conditions. With systematic implementation of the different dike setups towards a more reinforced dike, a gradual increase in the overall erosion resistance of the dike was achieved.

The implementation of reinforcement measures significantly altered erosion progression and generally improved hydraulic resistance. Specifically, using a 3D mesh mat together with non-woven geotextile was effective in reinforcing both vertical and horizontal transitions, leading to an increase of up to four times in the discharge capacity for vertical transitions. However, it should be noted that introducing geobuilding materials may locally disturb soil integrity and shift erosion-prone zones. Vegetation cover, particularly grass root systems in combination with the 3D mesh mat, further enhanced erosion resistance, approximately doubling hydraulic loading capacity in the tested configurations. Proper maintenance, along with construction and repair strategies, is crucial because localized repairs as well as excavated and recompacted zones can become preferential erosion hotspots. The repairs and appropriate recompaction should be carried out over sufficiently large areas to prevent significantly increased erosion volumes, which can be up to twice that of properly repaired areas.

Overall, while the 1:1 scale and use of real materials reduce scaling effects, limitations due to turf maturity, soil properties, construction sensitivity, and model effects must be considered when interpreting the results and their applicability to real dike systems. By ensuring optimized dike designs and constructions, the safety of the structures can be increased and their resilience for the future improved.

CRediT authorship contribution statement

Ina Schulte: Writing – original draft, Visualization, Methodology, Investigation, Formal analysis, Data curation, Conceptualization. **S. Harish:** Writing – review & editing, Visualization, Supervision, Conceptualization. **Nils Goseberg:** Writing – review & editing, Project administration, Funding acquisition. **Holger Schüttrumpf:** Writing – review & editing, Supervision, Project administration, Funding acquisition, Conceptualization.

Declaration of generative AI and AI-assisted technologies in the manuscript preparation process

During the preparation of this work, the author(s) used ChatGPT for editorial assistance and to improve readability. After using this tool/service, the author(s) reviewed and edited the output as needed and take full responsibility for the content of the published article.

Funding

This study was supported by the German Coastal Engineering Research Council KFKI and funded by the Federal Ministry of Research, Technology and Space (BMFTR) within the research project “Hydraulic stability, damage processes and prevention strategies for coastal protection structures at contact and transition points” (Grant Number 03F0925A-B). Open access funding provided by the Open Access Publishing Fund of RWTH Aachen University.

Declaration of competing interest

The authors declare that they have no known competing financial interests or personal relationships that could have appeared to influence the work reported in this paper.

Acknowledgement

The authors thank the technical staff for the construction of the dike model setups and for their help with the installation of measuring devices as well as Kisters AG for the loan and setup help of the surface radars. The authors also thank the two institutes PGG and GUT of RWTH Aachen University for their help with the characterization of the used dike cover material. The authors would also like to thank Naue GmbH & Co. KG for their valuable input on installation methods, supply and installation assistance for erosion protection systems. Finally, the first author likes to thank the students Lina Schone, Simon Bell, Sandra Bruggemann and Julian Wendt among others for their support during testing and evaluation.

Appendix A. Summary of studies on dike overflow and overtopping

The following table (Table A.1) summarizes existing model tests on dike overflow and overtopping erosion, presenting the applied hydraulic loads until test termination for different surface materials.

Table A.1
Summary of physical studies on overflow and wave overtopping with different surface materials.

Material		Load	Damage	Reference
Earthen materials	Different clays	Overtopping up to 10 l/(s*m)	Surface erosion, no failure	Möller et al. (2002)
	Clay, ash/silt, rolled turf vegetation	Overflow up to 500 l/(s*m)	Slip erosion	Olschewski et al. (2015)
	Fine-grained dredged materials, marsh clay	Overflow up to 550 l/(s*m)	Surface erosion	Cantré et al. (2017)
	Cohesive soil, lime-treated soil	Overflow up to 570 l/(s*m)	Scour, step stair erosion, no failure	Bonelli et al. (2018), Herrier et al. (2018)
	Gravel and sand	Overflow up to 72.5 l/(s*m)	Surface erosion, head-cut and breach	Pinettes et al. (2025)
Vegetation	Grass sods	Overtopping up to 30 l/(s*m)	No damage	Piontkowitz et al. (2009)
	Grass cover	Overtopping up to 120 l/(s*m)	Head-cut, roll-up, collapse	Trung (2014)
	Grass mixtures, bare clay, lime-stabilized clay, concrete blocks, erosion mat reinforcement	Overtopping up to 370 l/(s*m)	Damage depending on material	Thornton et al. (2014)
	Grass	Overtopping and overflow up to 170 l/(s*m)	Turf erosion, head-cut	van Damme et al. (2016)
	Grass mixtures	Overflow up to 215 l/(s*m)	Bare spots, no failure	Scheres and Schüttrumpf (2020)
	Natural grass, sandy silt, gravel	Overflow up to 140 l/(s*m)	No failure of grass, scouring and surface erosion of gravel	Picault et al. (2022)
Vegetation with transition	Grass cover, reinforced grass cover, clay and dikes with transitions	Overtopping up to 75 l/(s*m)	Erosion of the slope and at toe, gully erosion, head-cut, buldge out	van der Meer et al. (2010b), van der Meer (2008)
	Grass with transitions	Overtopping up to 75 l/(s*m)	Erosion at slope and toe	Steendam et al. (2011)
	Natural grass with transitions and reinforcement measures	Overflow up to 550 l/(s*m)	Collapse and head-cut erosion due to core sand mobilization through animal burrows	Koelewijn et al. (2022)
	Grass, clay and lime-treated clay with obstacle	Overtopping up to 190 l/(s*m)	Scour, no failure	Ebrahimi et al. (2025)
	Grass with transition and reinforcement measures	Overtopping up to 100 l/(s*m)	Erosion hole, failure of toe of horizontal berm, gully erosion, cliff erosion	van der Meer et al. (2025)

Appendix B. Detailed soil properties of the dike construction material

Table A.2 presents the material composition of the dike cover material used in this study in comparison with the German guideline EAK (2007) and from previous studies.

Table A.2
Comparison of material composition of dike cover soils.

Soil properties	EAK (2007)		Möller et al. (2002)			Present study
	EAK 93	**conditionally suitable**	**clay 1**	**clay 2**	**clay 3**	**clayey silt**
Clay content (%)	>10	10-15	35	20	10	10-17
Silt content (%)			53	45	30	77-83
Sand content (%)	<40	30-50	12	35	60	1-13
Yield point w_l (%)	>25	25-40				29.3
Plasticity number I_p (%)	>10	10-15				11.6
Installed water content w (%)	30-80	25-45				19.5
Dry density ρ_d (t/m^3)	0.85-1.45	1.25-1.55				1.69
Ignition loss V_{gl} (%)	<10	<5				2.31

Data availability

Data will be made available on request.

References

Achmus, Martin, Pohl, Martin, Schüttrumpf, Holger, Temmler, Helmut, 2019. Infiltrationsbedingte Prozesse in Der Abdeckung Von See- Und Ästuardeichen Und Deren Einfluss Auf Die Standsicherheit, 53. https://doi.org/10.18171/1.087113.

Baets, S. de, Poesen, J., Gyssels, G., Knapen, A., 2006. Effects of grass roots on the erodibility of topsoils during concentrated flow. Geomorphology 76 (1–2), 54–67. https://doi.org/10.1016/j.geomorph.2005.10.002.

Bernitt, Laurits, Lynett, Patrick, 2011. Breaching of sea dikes. In: Int. Conf. Coastal. Eng., p. 9. https://doi.org/10.9753/icce.v32.structures.9, 32.

Quantifying the erosion resistance of dikes with the overflowing simulator. In: Bonelli, S., Nicaise, S., Charrier, G., Chaouch, N., Byron, F., Grémeaux, Y. (Eds.), 2018. 3rd International Conference on Protection Against Overtopping. Grange-over-Sands, United Kingdom, 6-8 June.

Born, M.P., Brüll, C., Klopries, E.-M., Schüttrumpf, H., 2025. Überströmsichere Deiche an der Emscher - Endbericht (unpublished). RWTH Aachen University.

Briaud, J.-L., Chen, H.-C., Govindasamy, A.V., Storesund, R., 2008. Levee erosion by overtopping in New Orleans during the Katrina hurricane. J. Geotech. Geoenviron. Eng. 134 (5), 618–632. https://doi.org/10.1061/(ASCE)1090-0241(2008)134:5(618).

Cantré, Stefan, Olschewski, Jan, Saathoff, Fokke, 2017. Full-scale flume experiments to analyze the surface erosion resistance of dike embankments made of dredged materials. J. Waterway, Port, Coastal, Ocean Eng. 143 (3), 04017001. https://doi.org/10.1061/(ASCE)WW.1943-5460.0000375.

Chen, Chenghao, Mei, Shiang, Chen, Shengshui, Tang, Yi, Wan, Chengwei, 2022. Laboratory investigation of erosion behavior at the soil–structure interface affected by various structural factors. Nat. Hazards 111 (1), 1065–1084. https://doi.org/10.1007/s11069-021-05070-4.

Chu, J., Yan, S.W., Li, W., 2012. Innovative methods for dike construction – an overview. Geotext. Geomembranes 30, 35–42. https://doi.org/10.1016/j.geotexmem.2011.01.008.

CIRIA, 2013. In: The International Levee Handbook, C731. Construction Industry Research and Information Association, London, UK.

Depreiter, Davy, Vercruysse, Jeroen, Verelst, Kristof, Peeters, Patrik, 2025. Erosion resistance assessment of grass-covered embankments: insights from in situ overflow tests at the living lab hedwige-prosper polder. Water 17 (13), 2016. https://doi.org/10.3390/w17132016.

DIN 19712, 2013. Hochwasserschutzanlagen an Fließgewässern.

DIN 18125-2, 2020. Baugrund, Untersuchung Von Bodenproben - Bestimmung Der Dichte Des Bodens - Teil 2: Feldversuche.

DIN 18123-7, 2011. Baugrund, Untersuchung Von Bodenproben - Bestimmung Der Korngrößenverteilung.

DWA-M 507-1, 2011. Deiche an FließgewässernTeil 1: Planung, Bau und Betrieb, p. 2011.

EAK, 2007. Die Küste. Archiv für Forschung und Technik an der Nord- und Ostsee. EAK 2002 Korrigierte Ausgabe 2007. Die Küste 65, 1–589.

Ebrahimi, Masoumeh, van Damme, Myron, van Hemert, Henk, Soares-Frazão, Sandra, 2025. Close-range photogrammetry application to monitor levee erosion in case of wave overtopping. J. Hydraul. Eng. 151 (1), 04024057. https://doi.org/10.1061/JHEND8.HYENG-13897.

EurOtop, 2018. Manual on wave overtopping of sea defences and related structures. In: An Overtopping Manual Largely based on European Research, but for Worldwide Application. Available online at: http://www.overtopping-manual.com/.

Falkenrich, Pauline, Wilson, Jessica, Nistor, Ioan, Goseberg, Nils, Cornett, Andrew, Mohammadian, Abdolmajid, 2021. Nature-based coastal protection by large woody debris as compared to seawalls: a physical model study of beach morphology and wave reflection. Water 13 (15), 2020. https://doi.org/10.3390/w13152020.

Guo, Junke, 2015. Sidewall and non-uniformity corrections for flume experiments. J. Hydraul. Res. 53 (2), 218–229. https://doi.org/10.1080/00221686.2014.971449.

Heerten, G., Heibaum, M., Haselsteiner, R., Werth, K., 2008. Hochwasserbedrohungen - neue Sicherheiten im Deichbau mit Geokunststoffen. Vorträge Der Baugrundtagung 2008 in Dortmund. 30. Baugrundtagung Der DGGT. Dortmund, Germany, 24.-27. September. Deutsche Gesellschaft für Geotechnik e. V.

Heerten, G., Vollmert, L., 2013. Ideas for improved geotechnical structures for natural disaster mitigation. Proceedings of the 18th International Conference on Soil Mechanics and Geotechnical Engineering. 18th International Conference on Soil Mechanics and Geotechnical Engineering. Paris, pp. 1809–1812. International Society for Soil Mechanics and Geotechnical Engineering (ISSMGE). https://www.issmge.org/publications/publication/ideas-for-improved-geotechnical-structures-for-natural-disaster-mitigation.

Herrier, G., Bonelli, S., Cornacchioli, F., Nerincx, N., Nicaise, S., Puiatti, D., et al. (Eds.), 2018. Erosion Resistant Dikes Thanks to Soil Treatment with Lime. 3rd International Conference on Protection Against Overtopping. Grange-over-Sands, United Kingdom, 6-8 June.

Hewlett, H.W.M., Boorman, L.A., Bramley, M.E., 1987. Design of Reinforced Grass Waterways. Report 116.

Hiller, H., 1989. Der biotechnische Wert von standortgemäßen Grasnarben auf Flußdeichen – ansaatmischungen, Anlage und Pflege. In: Jahrbuch 4: Flußdeiche Und Flußdämme – Bewuchs Und Standsicherheit, pp. 119–152.

Hoffmans, G., 2012. The Influence of Turbulence on Soil Erosion. Delft: Eburon (Deltares select series, 10).

Hoffmans, G., van der Meer, G., Frissel, J., Paulissen, M., Verheij, H., Steendam, G.J., 2013. SBW Wave overtopping and grass cover strength. Predictions of Prototype Tests Nijmegen Millingen aan de Rijn. Deltares, 1206016-007.

Hoffmans, G., van Hoven, A., Hardeman, B., Verheij, H., 2015. Erosion of Grass Covers at Transitions and Objects on Dikes. https://doi.org/10.1201/b17703-84.

Igwe, P.U., Ezeukwu, J.C., Edoka, N.E., Ejie, O.C., Ifi, G.I., 2017. A review of vegetation cover as a natural factor to soil erosion. IJREH 1 (4), 21–28. https://doi.org/10.22161/ijreh.1.4.4.

Koelewijn, André R., Rikkert, Stephan J.H., Peeters, Patrik, Depreiter, Davy, van Damme, Myron, Zomer, Wouter, 2022. Overflow tests on grass-covered embankments at the living lab hedwige-prosperpolder: an overview. Water 14 (18), 2859. https://doi.org/10.3390/w14182859.

Kolb, A., Otremba, E., Brünger, W., 1962. Sturmflut 17. Februar 1962. Morphologie Der Deich- Und Flurbeschädigungen Zwischen Moorburg Und Cranz. Hamburger Geographische Studien, Heft 16. Universität Hamburg Institut für Geographie und Wirtschaftsgeographie, Hamburg.

Krebs, Verena, 2023. Innovationen Im Deichbau - Drei Verfahren Zur Erhöhung Der Deichsicherheit. Dissertation. RWTH Aachen University.

Le, Hai Trung, Verhagen, H.J., Vrijling, J.K., 2017. Damage to grass dikes due to wave overtopping. Nat. Hazards 86 (2), 849–875. https://doi.org/10.1007/s11069-016-2721-2.

Mehrtens, Björn, Vinkelau, Leon, Bölker, Thea, Lojek, Oliver, Ahrenbeck, Lukas, Schweiger, Constantin, et al., 2025. Benchmarking overview on methods for spatiotemporal detection of dune erosion in physical modeling. J. Waterway, Port, Coastal, Ocean Eng. 151 (4), 4025012. https://doi.org/10.1061/JWPED5.WWENG-2138, 04025012.

MMB, 2013. BAWMerkblatt Materialtransport im Boden. https://izw.baw.de/publikationen/merkblaetter/0/BAWMerkblatt_Materialtransport_im_Boden_MMB_2013.pdf.

Möller, J., Weissmann, R., Schüttrumpf, H., Grüne, J., Oumeraci, H., Richwien, W., Kudella, M., 2002. Interaction of wave overtopping and clay properties for seadikes. In: Scientific, World (Ed.), Coastal Engineering 2002. Proceedings of the 28th International Conference on Coastal Engineering. Solving Coastal Conundrums. with Assistance of Jane McKee Smith. ICCE 2002. U.S. Army Engineer Research and Development Center, Cardiff, Wales, pp. 2105–2115, 7-12 July.

Mozer, A., Born, M.P., Schüttrumpf, H., 2024. From sowing to flowing – integrating vegetation for indoor physical model tests in International Society of Offshore and Polar Engineering. In: Proceedings of the Fifteenth (2024) ISOPE Pacific-Asia Offshore Mechanics Symposium. Pacific-Asia Offshore Mechanics Symposium. Chennai, India, October 13-16, pp. 321–324.

Mulahasan, S., Al-Osmy, S., Alhashimi, S., 2021. Modelling of flow pattern in an open channel with sidewall obstruction. IOP Conf. Ser. Mater. Sci. Eng. 1090 (1), 12097. https://doi.org/10.1088/1757-899X/1090/1/012097.

Nandhini, D., Harish, S., Murali, K., Schüttrumpf, Holger, 2026. Numerical study of overflow hydrodynamics and pressure distribution on a spur dike under tidal bore-like flow. Appl. Ocean Res. 173, 105132. https://doi.org/10.1016/j.apor.2026.105132.

Olschewski, Jan, Cantre, Stefan, Saathoff, Fokke, Ossowski, Rafał, 2015. Overflowing tests at the polish DREDGDIKES research dike – stability of the dike surface against erosion. Eng. Struct. Technol. 6 (4), 159–168. https://doi.org/10.3846/2029882X.2015.1074528.

Oumeraci, H., Möller, J., Schüttrumpf, H., Richwien, W., Weissmann, R., 2001. Belastung der Binnenböschung von Seedeichen durch Wellenüberlauf. Abschlußbericht -. LWI Bericht Nr. 872. Braunschweig/Essen.

Pan, Yi, Li, Lin, Amini, Farshad, Kuang, Cuiping, 2015. Overtopping erosion and failure mechanism of earthen levee strengthened by vegetated HPTRM system. Ocean Eng. 96, 139–148. https://doi.org/10.1016/j.oceaneng.2014.12.012.

Peeters, Patrik, Vos, Leen de, Vandevoorde, Bart, van der Meer, Jentsje, 2013. Application of grass cover failure models following in situ wave overtopping experiments in Belgium. ujg 1 (2), 46–55. https://doi.org/10.13189/ujg.2013.010202.

Picault, Christophe, Campette, Fabrice, Bonelli, Stéphane, Nicaise, Sylvie, Chaouch, Naim, Byron, Faustine, et al., 2022. Field Testing of the Overflow Erosion of Rhone River Levees.

Pinettes, Patrick, Haddad, Hanna, Picault, Christophe, Bonelli, Stéphane, Courivaud, Jean-Robert, Mallet, Thibaut, 2025. Two erosion tests to quantify resistance to erosion during overflow: the jet erosion test and the overflow test. In: CIGB, I.C.O.L.D. (Ed.), Twenty-Eighth International Congress on Large Dams/Vingt-Huitième Congrès International Des Grands Barrages. CRC Press, London, pp. 1860–1881.

Piontkowitz, T., Verhagen, H.J., Verheij, H., Mai Cao, T., Dassanayake, D., Roelvink, D., et al., 2009. EroGRASS - failure of grass cover layers at seaward and shoreward dike slopes. Design, Construct. Experim. Perform. Available online at: https://kyst.dk/media/fwkjel1w/erograss_report_a_final.pdf.

Ponsioen, Luc, van Damme, Myron, Hofland, Bas, Peeters, Patrik, 2019. Relating grass failure on the landside slope to wave overtopping induced excess normal stresses. Coast. Eng. 148, 49–56. https://doi.org/10.1016/j.coastaleng.2018.12.009.

Powledge, George R., Ralston, David C., Miller, Paul, Chen, Yung Hai, Clopper, Paul E., Temple, D.M., 1989. Mechanics of overflow erosion on embankments. I: research activities. J. Hydraul. Eng. 115 (8), 1040–1055. https://doi.org/10.1061/(ASCE)0733-9429(1989)115:8(1040).

Richwien, W., Pohl, C., Vavrina, L., Weißmann, R., Sparboom, U., 2010. Integrierte Bemessung von See- und Ästuardeichen. Abschlussbericht Des Teilprojekts INTBEM

A Analyse Bodenmechanischer Prozesse Zur Funktionalen Optimierung Von Deichelementen.
Robin, Arif Hasan Khan, Irving, Louis John, Crush, Jim, Schnyder, Hans, Lattanzi, Fernando Alfredo, Matthew, Cory, 2021. Time course of root axis elongation and lateral root formation in perennial ryegrass (Lolium perenne L.). Plants (Basel, Switzerland) 10 (8). https://doi.org/10.3390/plants10081677.
Sanchez-Arcilla, Agustin (Ed.), 2006. Coastal Dynamics 2005. Fifth International Conference on Coastal Dynamics. Barcelona, Spain, April 4-8, 2005. American Society of Civil Engineers, Reston, VA.
Scheres, B., Schüttrumpf, H., 2020. Investigating the erosion resistance of different vegetated surfaces for ecological enhancement of sea dikes. JMSE 8 (7), 519. https://doi.org/10.3390/jmse8070519.
Schulte, Ina, Rodermund, Henrike, Selvam, Harish, Becker, Jessica, Schweiger, Constantin, Schürenkamp, David, et al., 2024. Inventory of transitions on sea dikes at the German coast: spatial analysis, design and damages. Front. Built Environ. 10, 1468726. https://doi.org/10.3389/fbuil.2024.1468726.
Schüttrumpf, H., Oumeraci, H., 2002. Schäden an See- und Stromdeichen. Leichtweiss-Institut für Wasserbau der Technischen Universität Braunschweig 129–171. Mitteilungen, Heft 149 (Heft 149).
Schüttrumpf, H., Oumeraci, H., 2004. Learning from seadike failures. PIANC Bulletin 117, 47–60.
Schüttrumpf, H., Scheres, B. (Eds.), 2020. Ökologische Aufwertung Von Seedeichsystemen. Erste Planungsempfehlungen Für Die Praxis Mit Aktuellen Erkenntnissen Aus Der Wissenschaft, first ed. 2020. Springer Fachmedien Wiesbaden; Imprint Springer Vieweg, Wiesbaden.
Schüttrumpf, Holger, Oumeraci, Hocine, 2005. Layer thicknesses and velocities of wave overtopping flow at seadikes. Coast. Eng. 52 (6), 473–495. https://doi.org/10.1016/j.coastaleng.2005.02.002.
Sprangers, J.T.C.M., 1999. Vegetation Dynamics and Erosion Resistance of Sea Dyke Grassland. Wageningen Agricultural University, Wageningen, the Netherlands. PhD thesis.
Stanczak, Grzegorz, 2008. Breaching of Sea Dikes Initiated from the Seaside by Breaking Wave Impacts. Technische Universität Braunschweig and University of Florence, Braunschweig. Dissertation.
Steendam, G.J., Provoost, Y., van der Meer, J., 2012. Destructive wave overtopping and wave run-up tests on grass covered slopes of real dikes. Coast. Eng. Proc. 1 (33), 64. https://doi.org/10.9753/icce.v33.structures.64.
Steendam, G.J., van der Meer, J.W., Hardeman, B., van Hoven, A., 2011. Destructive wave overtopping tests on grass covered landward slopes of dikes and transitions to berms. Coast. Eng. Proc. 1 (32), 8. https://doi.org/10.9753/icce.v32.structures.8.
TAW, 1996. Clay for dikes. Road and Hydraulic Engineering Institute of the Directorate General of Public Works and Water Management (RWS-DWW). Technical Advisory Committee on Water Defences. Delft.
TAW, 1998. Erosiebestendigheid Van Grasland Als Dijkbekleding.
TAW, 1999. Guide on Sea and Lake Dikes 1999.
TAW, 2002. Technical Report Wave run-up and Wave Overtopping at Dikes.
Thornton, C., Hughes, S., Scholl, B., Youngblood, N., 2014. Estimating grass slope resiliency during wave overtopping: results from full-scale overtopping simulator testing. Coast. Eng. Proc. 1 (34). https://doi.org/10.9753/icce.v34.structures.52.
Trung, L.H., 2014. Overtopping on Grass Covered Dikes. Resistance and Failure of the Inner Slopes. Dissertation. Delft University of Technology, Delft.
Utley, B.C., Wynn, T.M., 2008. Cohesive soil erosion: theory and practice. In: Babcock, Jr.Roger W., Walton, Raymond (Eds.), World Environmental and Water Resources Congress 2008. World Environmental and Water Resources Congress 2008. Honolulu, Hawaii, United States, May 12-16, 2008. American Society of Civil Engineers, Reston, VA, pp. 1–10.
van Baars, S., van Kempen, I.M., 2009. The causes and mechanisms of historical dike failures in the Netherlands. E-WAter.
van Bergeijk, Vera, Zwanenburg, Suzanna, Nieuwenhuis, Jan-Willem, Jong, Kees de, van der Meer, Martin, Halter, Werner, et al., 2025. Erosion process of a clay revetment with grass cover on coastal flood defences based on large scale physical model tests. Int. Conf. Coastal. Eng. 38, 28. https://doi.org/10.9753/icce.v38.papers.28.
van Bergeijk, V.M., Verdonk, Vincent A., Warmink, Jord J., Hulscher, Suzanne J.M. H., 2021. The cross-dike failure probability by wave overtopping over grass-covered and damaged dikes. Water 13 (5), 690. https://doi.org/10.3390/w13050690.
van Bergeijk, V.M., Warmink, J., Hulscher, S., 2022a. The effects of transitions in cover type and height on the wave overtopping load on grass-covered flood defences. Appl. Ocean Res. 125, 1–17. https://doi.org/10.1016/j.apor.2022.103220.
van Bergeijk, V.M., Warmink, Jord J., Hulscher, Suzanne J.M.H., 2022b. The wave overtopping load on landward slopes of grass-covered flood defences: deriving practical formulations using a numerical model. Coast. Eng. 171, 104047. https://doi.org/10.1016/j.coastaleng.2021.104047.
van Damme, Myron, Ponsioen, Luc, Herrero, Monica, Peeters, Patrik, 2016. Comparing overflow and wave-overtopping induced breach initiation mechanisms in an embankment breach experiment. E3S Web Conf 7, 3004. https://doi.org/10.1051/e3sconf/20160703004.
van der Meer, J., 2008. Erosion strength of inner slopes of dikes against wave overtopping. Preliminary Conclusions After Two Years of Testing with the Wave Overtopping Simulator.
van der Meer, J., Hardeman, B., Steendam, G.J., Schüttrumpf, H., Verheij, H., 2010a. Flow depths and velocities at crest and landward slope of a dike, in theory and with the wave overtopping simulator. Coast. Eng. Proc. 1 (32), 10.
van der Meer, J., Schrijver, R., Hardeman, B., van Hoven, A., Verheij, H., Steendam, G.J., 2010b. Guidance on erosion resistance of inner slopes of dikes from three years of testing with the wave overtopping simulator. In: Allsop, W. (Ed.), Coast, Marine Structures and Breakwaters: Adapting Change. Thomas Telford Ltd., London, UK, pp. 460–473. https://doi.org/10.1680/cmsb.41318.0044.
van der Meer, J., van Hoven, A., Paulissen, M., Steendam, G.J., Verheij, H., Hoffmans, G., Kruse, G., 2012. Handreiking. Toetsen Grasbekledingen Op Dijken t.b.v. Het Opstellen Van Het Beheerdersoordeel (BO) in De Verlegde Derde Toetsronde. Rijkswaterstaat.
van der Meer, Jentsje, Hardeman, Bianca, Valk, Jan, Versteeg, Stanley, Veld, Martijn Huis in't, Halter, Werner, et al., 2025. Improving transitions at grass covered dike slopes using the wave overtopping simulator. In: 38Int. Conf. Coastal. Eng., p. 22. https://doi.org/10.9753/icce.v38.papers.22.
van der Vegt, Niels, Warmink, Jord J., Hofland, Bas, van, Bergeijk, Vera, M., Hulscher, Suzanne J.M.H., 2025. Variation in flow characteristics of overtopping waves on dike crests. Coast. Eng. 201, 104772. https://doi.org/10.1016/j.coastaleng.2025.104772.
van Steeg, P., van Hoven, A., 2013a. Overgangen bij grasbekledingen in primaire waterkeringne. Aanzet tot oplossingsrichtingen. Deltares, 1208394-000.
van Steeg, P., van Hoven, A., 2013b. Overgangen en overgangsconstructies. Deltares, 1208394-000.
Vannoppen, Wouter, Poesen, Jean, Peeters, Patrik, Baets, Sarah de, Vandevoorde, Bart, 2016. Root properties of vegetation communities and their impact on the erosion resistance of river dikes. Earth Surf. Process. Landf. 41 (14), 2038–2046. https://doi.org/10.1002/esp.3970.
Verheij, H., Hoffmans, G., Hardeman, B., Paulissen, M. (Eds.), 2012. Erosion at Transitions in Landward Slopes of Dikes due to Wave Overtopping. ISCE6-2012 - Sixth International Conference on Scour Ans Erosion. Paris, 27.-31. August.
Werth, K., Haselsteiner, R., Steinbacher, F., 2011. Overtopping and overflow of flood protection embankments – risk reduction of embankment dam failure by the use of geosynthetics. In: Vogt, Norbert, Schuppener, Bernd, Straub, Daniel, Bräu, Gerhard (Eds.), Proceedings of the 3rd International Symposium on Geotechnical Safety and Risk. ISGSR 2011. Munich, Germany, 2-3 June. Bundesanstalt für Wasserbau, Karlsruhe, pp. 597–604.
Xie, Quanyi, Liu, Jian, Han, Bo, Li, Hongtao, Li, Yuying, Li, Xuanzheng, 2018. Critical hydraulic gradient of internal erosion at the soil–structure interface. Processes 6 (7), 92. https://doi.org/10.3390/pr6070092.
Zanke, Ulrich, 2013. Hydraulik für den Wasserbau. Springer Berlin Heidelberg.
Zhang, Zihan, Li, Changdong, Ye, Yang, 2025. Meso-Structural evolution and erosion mechanisms of soil-structure interface explored via In-Situ CT scanning. J. Hydrol. 658, 133128. https://doi.org/10.1016/j.jhydrol.2025.133128.
Zhao, G., 2016. Breach Growth in Cohesive Embankments due to Overtopping. Dissertation. Delft University of Technology. https://doi.org/10.4233/uuid:ee435ef7-f71c-493c-812b-68cf1e39aa33.